J. Fluid Mech. (2013), *vol.* 721, *pp.* 541–577. © Cambridge University Press 2013
doi:10.1017/jfm.2013.81

An explicit algebraic model for the subgrid-scale passive scalar flux

Amin Rasam†, Geert Brethouwer and Arne V. Johansson

Linné FLOW Centre, KTH Mechanics, SE-100 44 Stockholm, Sweden

(Received 28 March 2012; revised 1 February 2013; accepted 4 February 2013;
first published online 18 March 2013)

In Marstorp *et al.* (*J. Fluid Mech.*, vol. 639, 2009, pp. 403–432), an explicit algebraic subgrid stress model (EASSM) for large-eddy simulation (LES) was proposed, which was shown to considerably improve LES predictions of rotating and non-rotating turbulent channel flow. In this paper, we extend that work and present a new explicit algebraic subgrid scalar flux model (EASSFM) for LES, based on the modelled transport equation of the subgrid-scale (SGS) scalar flux. The new model is derived using the same kind of methodology that leads to the explicit algebraic scalar flux model of Wikström *et al.* (*Phys. Fluids*, vol. 12, 2000, pp. 688–702). The algebraic form is based on a weak equilibrium assumption and leads to a model that depends on the resolved strain-rate and rotation-rate tensors, the resolved scalar-gradient vector and, importantly, the SGS stress tensor. An accurate prediction of the SGS scalar flux is consequently strongly dependent on an accurate description of the SGS stresses. The new EASSFM is therefore primarily used in connection with the EASSM, since this model can accurately predict SGS stresses. The resulting SGS scalar flux is not necessarily aligned with the resolved scalar gradient, and the inherent dependence on the resolved rotation-rate tensor makes the model suitable for LES of rotating flow applications. The new EASSFM (together with the EASSM) is validated for the case of passive scalar transport in a fully developed turbulent channel flow with and without system rotation. LES results with the new model show good agreement with direct numerical simulation data for both cases. The new model predictions are also compared to those of the dynamic eddy diffusivity model (DEDM) and improvements are observed in the prediction of the resolved and SGS scalar quantities. In the non-rotating case, the model performance is studied at all relevant resolutions, showing that its predictions of the Nusselt number are much less dependent on the grid resolution and are more accurate. In channel flow with wall-normal rotation, where all the SGS stresses and fluxes are non-zero, the new model shows significant improvements over the DEDM predictions of the resolved and SGS quantities.

Key words: rotating turbulence, turbulence modelling, turbulent flows

1. Introduction

Passive scalar mixing in turbulent flows is of importance in many industrial applications and environmental processes. A passive scalar is advected and mixed, but has no effect on the flow and can represent, for example, a pollutant carried by

† Email address for correspondence: rasam@mech.kth.se

https://doi.org/10.1017/jfm.2013.81 Published online by Cambridge University Press

the flow or small temperature fluctuations. Knowledge of passive scalar mixing is also a first step towards the understanding of reactive flows where the mixing of different species plays an important role. Large-eddy simulation (LES) is a promising tool to predict mixing of scalars in turbulent flows (Lesieur & Métais 1996; Meneveau & Katz 2000). Moreover, it has the potential to predict turbulent scalar transport in rotating flows (Marstorp, Brethouwer & Johansson 2007), while this is difficult for other scalar transport models.

In the Reynolds-averaged Navier–Stokes (RANS) approach, the eddy diffusivity model (EDM) has been widely used for the prediction of the turbulent scalar flux, in spite of its shortcomings, which have been pointed out in many papers (Johansson & Wikström 1999; Wikström, Wallin & Johansson 2000). In LES, the EDM is also often used for the prediction of the subgrid scalar flux, since it is computationally inexpensive and is easy to implement. However, it suffers from the same drawbacks as in the RANS method (Yoshizawa 1988; Kang & Meneveau 2001; Peng & Davidson 2002; Sagaut 2010). Since the EDM assumes the subgrid-scale (SGS) scalar flux vector to be aligned with the resolved scalar gradient vector, it cannot predict the anisotropy of SGS scalar flux arising from the mean velocity gradient. Kang & Meneveau (2001) used experimental data on the wake of a heated cylinder and showed that, in an *a priori* test, the EDM predicts an almost isotropic mean scalar variance SGS dissipation, while the real SGS dissipation tensor computed from the filtered experimental data is anisotropic at all relevant filter sizes.

Improvements over the EDM have been reported for scale similarity and gradient SGS scalar flux models, which are similar to their counterparts for SGS stresses – see Bardina, Ferziger & Reynolds (1989) and Clark, Ferziger & Reynolds (1979), respectively. These models improve the direction of the predicted SGS scalar flux vector but are not dissipative enough. Therefore, they are often combined with an eddy diffusivity term. Salvetti & Banerjee (1995) proposed a mixed scale similarity model, which leads to a tensor EDM. Jiménez, Valiño & Dopazo (2001*b*) have shown that such a model improves the description of the scalar variance transfer compared to the EDM. The concept of tensor eddy diffusion was originally proposed by Batchelor (1949) for RANS modelling. An example of a mixed dynamic eddy diffusivity and dynamic gradient SGS scalar flux model is the model by Porté-agel *et al.* (2001*a*). This model has been used in *a priori* analysis of LES of atmospheric flows (Porté-agel *et al.* 2001*a*,*b*; Higgins, Parlange & Meneveau 2004) and the wake of a heated cylinder in a wind tunnel (Kang & Meneveau 2001, 2002).

Peng & Davidson (2002) proposed a nonlinear tensor EDM with a tensor diffusivity proportional to the resolved strain-rate tensor, and tested their model for LES of buoyancy-driven turbulent flow between two differentially heated vertical walls. Their model improved LES predictions of some statistics compared to the EDM. A recent example of a mixed nonlinear SGS scalar flux model is the dynamic tensor EDM by Wang *et al.* (2008). Their model consists of a standard eddy diffusivity part and a tensor eddy diffusivity part, which is a quadratic tensor function of the resolved strain-rate tensor. Their model improved LES predictions of the SGS scalar fluxes in comparison with the EDM.

Resolution requirements for LES have been discussed in many papers (Baggett, Jiménez & Kravchenko 1997; Davidson 2009; Choi & Moin 2012). In free shear flows, the resolution requirements are less strict for LES since the degree of anisotropy in the flow does not scale with the Reynolds number (Baggett *et al.* 1997), and the SGS motions tend to be more isotropic and can be represented reasonably well by many SGS models. However, in wall-bounded flows, the presence of the wall results

https://doi.org/10.1017/jfm.2013.81 Published online by Cambridge University Press

in a decrease of the integral length scale, which substantially increases the degree of anisotropy of the turbulence in the near-wall region. This anisotropy has to be resolved by the grid, resulting in higher computational costs, or has to be properly represented in the form of anisotropy in the SGS motions by a proper SGS model. The increase in the computational costs, following the former approach, scales largely with the Reynolds number ($\sim Re^{26/14}$) so that the cost of a wall-resolved LES with an SGS model with an isotropic eddy viscosity type of formulation approaches that of the direct numerical simulation (DNS) ($\sim Re^{37/14}$) (see Choi & Moin 2012). These requirements in wall-bounded flows motivate the development of new SGS models, for both stresses and scalar fluxes, that are able to represent the SGS anisotropy better. LES would then be possible for a larger range of applications with a lower computational cost.

In Marstorp *et al.* (2009), we developed an explicit algebraic subgrid stress model (EASSM) that substantially improves the description of the individual SGS stresses in comparison with isotropic eddy viscosity models. Further investigations (Rasam *et al.* 2011*a*,*b*) show that the EASSM predictions are much less sensitive to the grid resolution and more accurate than the dynamic eddy viscosity model (DEVM). The next step, which is taken in this paper, is applying similar ideas to the subgrid scalar flux modelling. Wikström *et al.* (2000) proposed an explicit algebraic scalar flux model (EASFM) based on a modelled transport equation for the Reynolds-averaged scalar flux. The EASFM predicts the scalar flux more accurately in shear flows than the EDM. By applying the same kind of methodology that leads to the EASFM for the Reynolds-averaged scalar flux, we develop a new explicit algebraic subgrid scalar flux model (EASSFM) for LES. The new EASSFM includes information about the SGS stresses, the resolved strain-rate and rotation-rate tensors and is expected to improve the description of the individual SGS scalar flux components. The predicted SGS scalar flux in the EASSFM is only partly aligned with the resolved scalar gradient, and the model can thus be regarded as a mixed model derived from a modelled transport equation.

Similar to the eddy viscosity SGS stress model predictions for the velocity field, the EDM predictions of the scalar field are sensitive to the resolution, owing to its formulation. The new EASSFM provides for similar improvements in the description of the individual SGS fluxes as the EASSM for the SGS stresses and leads to LES predictions that are less sensitive to the grid resolution and, in general, more accurate compared to the EDM.

In order to validate the new model, we perform LES of scalar transport in channel flow without rotation and with wall-normal rotation. Turbulent channel flows with system rotation have been studied by several authors using LES. Examples of LES of channel flow with spanwise system rotation are the works by Tafti & Vanka (1991) and Piomelli & Liu (1995), where in the former the eddy viscosity model with near-wall damping has been used and in the latter a localized DEVM has been proposed. The work by Tsubokura *et al.* (1999) is another example where the SGS model by Yoshizawa *et al.* (1996) has been used for LES of turbulent channel flow with spanwise system rotation. LES of turbulent channel flow with streamwise system rotation has been carried out by Oberlack *et al.* (2006), where it has been shown that the DEVM does not perform well. Marstorp *et al.* (2009) used the EASSM for LES of channel flow with spanwise and streamwise system rotation and showed that their model significantly improves LES predictions over the DEVM in both cases.

This paper is organized as follows. In § 2 the governing equations of LES in a rotating frame of reference are introduced. The derivation of the new model is

https://doi.org/10.1017/jfm.2013.81 Published online by Cambridge University Press

presented in § 3. In § 4, details of the numerical method and the SGS stress and scalar flux models are introduced. Simulation results for the non-rotating channel flow are given and discussed in § 5, which is followed by a discussion about the SGS activity analysis in § 6. In § 7, LES results of channel flow with wall-normal system rotation are presented and discussed; finally, in § 8 the conclusions are drawn.

2. Governing equations of LES

The governing equations of LES are obtained by filtering the Navier–Stokes, continuity and scalar transport equations. In a rotating frame of reference, these equations read

$$\frac{\partial \widetilde{u}_i}{\partial t} + \widetilde{u}_j \frac{\partial \widetilde{u}_i}{\partial x_j} = -\frac{1}{\rho}\frac{\partial \widetilde{p}}{\partial x_i} + \nu \frac{\partial^2 \widetilde{u}_i}{\partial x_k \partial x_k} - 2\epsilon_{ijk}\Omega_j \widetilde{u}_k - \frac{\partial \tau_{ij}}{\partial x_j}, \tag{2.1}$$

$$\frac{\partial \widetilde{u}_i}{\partial x_i} = 0, \tag{2.2}$$

$$\frac{\partial \widetilde{\theta}}{\partial t} + \widetilde{u}_j \frac{\partial \widetilde{\theta}}{\partial x_j} = \frac{\nu}{Pr}\frac{\partial^2 \widetilde{\theta}}{\partial x_k \partial x_k} - \frac{\partial q_j}{\partial x_j}, \tag{2.3}$$

where $\widetilde{\ }$ denotes a grid-filtered quantity, $\widetilde{u}_i$ and $\widetilde{\theta}$ denote the filtered velocity vector and passive scalar, respectively, and $\widetilde{p}$ includes both the filtered pressure and the centrifugal force. The third term on the right-hand side in (2.1) is the Coriolis force, Ω_j is the system rotation vector and ϵ_{ijk} is the alternating tensor. The remaining symbols are the kinematic viscosity ν, the Prandtl number Pr and a constant density ρ. The summation convention is used for repeated indices. The SGS stress tensor and the SGS scalar flux vector are defined as

$$\tau_{ij} = \widetilde{u_i u_j} - \widetilde{u}_i \widetilde{u}_j, \quad q_i = \widetilde{u_i \theta} - \widetilde{u}_i \widetilde{\theta}, \tag{2.4}$$

which have to be modelled in order to close the set of equations.

3. Subgrid model development

3.1. *Derivation of the model*

The new subgrid scalar flux model is derived in the same way as the EASFM of Wikström *et al.* (2000) but from the transport equation of the SGS scalar fluxes. In an inertial frame of reference, this transport equation is written as

$$\frac{\mathrm{D}q_i}{\mathrm{D}t} = P^{SGS}_{i\theta} + D^{SGS}_{i\theta} + \Pi^{SGS}_{i\theta} - \epsilon^{SGS}_{i\theta}, \tag{3.1}$$

where $P^{SGS}_{i\theta}$ is the production of subgrid scalar flux by the interaction of the subgrid scalar fluxes and the resolved velocity gradients and the interaction of the SGS stresses with the resolved scalar gradients. The production term $P^{SGS}_{i\theta}$ represents the actual SGS dissipation and appears as a closed term in the equations. The term $\Pi^{SGS}_{i\theta}$ is the subgrid pressure scalar-gradient correlation and $\epsilon^{SGS}_{i\theta}$ is the molecular subgrid scalar flux dissipation, both of which are unclosed terms and need to be modelled. Using the Germano notation (Germano 1992) for brevity in the formulation, $\mathscr{T}(a, b) = \widetilde{ab} - \widetilde{a}\widetilde{b}$, we can write these terms as

$$P^{SGS}_{i\theta} = -q_j \frac{\partial \widetilde{u}_i}{\partial x_j} - \tau_{ij}\frac{\partial \widetilde{\theta}}{\partial x_j}, \tag{3.2}$$

https://doi.org/10.1017/jfm.2013.81 Published online by Cambridge University Press

$$\Pi_{i\theta}^{SGS} = \frac{1}{\rho}\mathscr{T}\left(p, \frac{\partial\theta}{\partial x_i}\right), \tag{3.3}$$

$$\epsilon_{i\theta}^{SGS} = \left(\nu + \frac{\nu}{Pr}\right)\mathscr{T}\left(\frac{\partial\theta}{\partial x_j}, \frac{\partial u_i}{\partial x_j}\right). \tag{3.4}$$

The diffusion term, $D_{i\theta}^{SGS}$, in (3.1) includes both turbulent and molecular diffusion of the subgrid scalar flux and is given by

$$D_{i\theta}^{SGS} = \frac{\partial}{\partial x_j}\left(-\frac{\delta_{ij}}{\rho}\mathscr{T}(\theta, p) - \mathscr{T}(u_j, u_i\theta) + \nu\mathscr{T}\left(\theta, \frac{\partial u_i}{\partial x_j}\right) + \frac{\nu}{Pr}\mathscr{T}\left(u_i, \frac{\partial\theta}{\partial x_j}\right) - q_j\widetilde{u}_i - \tau_{ij}\widetilde{\theta}\right), \tag{3.5}$$

where δ_{ij} is the Kronecker delta.

In analogy with the EASFM, we normalize the subgrid scalar flux with the SGS kinetic energy, K^{SGS}, and SGS scalar intensity, K_θ^{SGS}, as

$$\xi_i = \frac{q_i}{\sqrt{K^{SGS}K_\theta^{SGS}}}, \quad K^{SGS} = \frac{1}{2}(\widetilde{u_i u_i} - \widetilde{u}_i\widetilde{u}_i), \quad K_\theta^{SGS} = \frac{1}{2}(\widetilde{\theta\theta} - \widetilde{\theta}\widetilde{\theta}). \tag{3.6}$$

The transport equation for the normalized subgrid scalar flux, ξ_i, reads

$$\frac{\mathrm{D}\xi_i}{\mathrm{D}t} - D_i^\xi = -\frac{1}{2}\xi_i\left(\frac{P_\theta^{SGS} - \epsilon_\theta^{SGS}}{K_\theta^{SGS}} + \frac{P_K^{SGS} - \epsilon_K^{SGS}}{K^{SGS}}\right) + \frac{P_{i\theta}^{SGS} - \epsilon_{i\theta}^{SGS} + \Pi_{i\theta}^{SGS}}{\sqrt{K^{SGS}K_\theta^{SGS}}}, \tag{3.7}$$

where P_K^{SGS} and ϵ_K^{SGS} are the production and the dissipation of K^{SGS}, respectively, P_θ^{SGS} and ϵ_θ^{SGS} denote the production and the dissipation of K_θ^{SGS}, respectively, and D_i^ξ is the diffusion of ξ_i.

The weak equilibrium assumption, introduced by Rodi for the Reynolds stresses (Rodi 1972, 1976), is an essential part in the derivation of the explicit algebraic models (Wallin & Johansson 2000; Wikström *et al.* 2000; Grundestam, Wallin & Johansson 2005). In the RANS context, it states that the advection and diffusion of the normalized Reynolds stresses can be neglected. This assumption is fully satisfied in homogeneous turbulent flows in equilibrium and to a high degree in regions of inhomogeneous turbulent flows where the deviation from parallel flow is small, e.g. the near-wall region of a boundary layer. In Marstorp *et al.* (2009), we used the weak equilibrium assumption for the normalized anisotropy of the SGS stresses and derived the EASSM. The weak equilibrium assumption for the normalized scalar flux vector is similar to that for the Reynolds stresses and was used in the derivation of the EASFM by Wikström *et al.* (2000). Here, we use this assumption for the normalized subgrid scalar fluxes, i.e. we assume that the left-hand side of (3.7) is negligible,

$$\frac{\mathrm{D}\xi_i}{\mathrm{D}t} - D_i^\xi = 0. \tag{3.8}$$

In § 3.2 we extend the model to rotating frames of reference and in § 3.5, we evaluate the validity of the weak equilibrium assumption for the LES of the scalar field in a non-rotating frame of reference.

In order to further develop the model, we need to introduce a model for $\Pi_{i\theta}^{SGS}$ in (3.3). An exact integral solution can be found for the pressure scalar-gradient correlation term from the instantaneous transport equation of the scalar and the momentum equations, using Green's function (Shih & Lumley 1986). The model that

https://doi.org/10.1017/jfm.2013.81 Published online by Cambridge University Press

is usually used in the RANS community for this term is based on the interpretation of different terms in this integral expression. The dissipation term is also lumped into this term and modelling is done for these two terms together.

We employ the model that is used by Wikström *et al.* (2000) and rewrite it for $\Pi_{i\theta}^{SGS} - \epsilon_{i\theta}^{SGS}$ in terms of q_i, τ_{ij} and filtered gradients instead of Reynolds-averaged correlations and mean gradients. This approach leads to

$$\Pi_{i\theta}^{SGS} - \epsilon_{i\theta}^{SGS} = -c_{1\theta} q_i \frac{\epsilon_K^{SGS}}{K^{SGS}} + c_{2\theta} q_j \frac{\partial \widetilde{u}_i}{\partial x_j} + c_{3\theta} q_j \frac{\partial \widetilde{u}_j}{\partial x_i} + c_{4\theta} \tau_{ij} \frac{\partial \widetilde{\theta}}{\partial x_j}, \tag{3.9}$$

where the first term on the right-hand side represents a model for the turbulence–turbulence interaction (also called slow term). Monin (1965) proposed this model for the RANS, which is based on Rotta's return to isotropy concept with $c_{1\theta}$ known as the Rotta coefficient (see e.g. Pope 2000). The $c_{1\theta}$ coefficient is later computed *a priori* using DNS data and the return to isotropy concept in § 3.3. The original model by Wikström *et al.* (2000) also contains another slow term, which involves the time scale of the scalar field as $q_i(\epsilon_\theta^{SGS}/K_\theta^{SGS})$. For the SGS model, this term can be approximated as $q_i(\epsilon_K^{SGS}/K^{SGS})/Pr$, where the model $(\epsilon_K^{SGS}/K^{SGS})/(\epsilon_\theta^{SGS}/K_\theta^{SGS}) = Pr$ (Jiménez *et al.* 2001*a*) has been used. Therefore, its effect is similar to the first term on the right-hand side of (3.9) and can be seen as included in the first term.

Other terms in the model (3.9) represent interactions between resolved and SGS quantities (also called rapid terms), where $c_{2\theta}$, $c_{3\theta}$ and $c_{4\theta}$ are the corresponding model coefficients and are given in § 3.3. The role of these terms is to counterbalance the rate of production of the subgrid scalar flux.

We further use the assumptions $P_\theta^{SGS} = \epsilon_\theta^{SGS}$ and $P_K^{SGS} = \epsilon_K^{SGS}$ implying that the production and dissipation of the SGS kinetic energy and SGS scalar intensity are locally in balance. The former assumption was used in the development of the EASSM. These assumptions considerably simplify the formulation and are validated in § 3.4.

Using the model (3.9) along with the weak equilibrium assumption and using $P_\theta^{SGS} = \epsilon_\theta^{SGS}$ and $P_K^{SGS} = \epsilon_K^{SGS}$, we obtain a linear system of equations for the subgrid scalar flux

$$A_{ij} q_j = -(1 - c_{4\theta}) \tau^* \tau_{ij} \frac{\partial \widetilde{\theta}}{\partial x_j}, \tag{3.10}$$

where

$$A_{ij} = c_{1\theta} \delta_{ij} + c_S \widetilde{S}_{ij}^* + c_\Omega \widetilde{\Omega}_{ij}^* \tag{3.11}$$

and $\tau^* = K^{SGS}/\epsilon_K^{SGS}$ is the time scale of the subgrid velocity field and needs to be modelled (see § 4.2). The model coefficients $c_{2\theta}$ and $c_{3\theta}$ are reorganized as $c_S = (1 - c_{2\theta} - c_{3\theta})$ and $c_\Omega = (1 - c_{2\theta} + c_{3\theta})$. The normalized filtered strain-rate and rotation-rate tensors are defined as

$$\widetilde{S}_{ij}^* = \frac{\tau^*}{2}\left(\frac{\partial \widetilde{u}_i}{\partial x_j} + \frac{\partial \widetilde{u}_j}{\partial x_i}\right), \quad \widetilde{\Omega}_{ij}^* = \frac{\tau^*}{2}\left(\frac{\partial \widetilde{u}_i}{\partial x_j} - \frac{\partial \widetilde{u}_j}{\partial x_i}\right). \tag{3.12}$$

If A_{ij} in (3.10) is inverted, we obtain the EASSFM for the subgrid scalar flux vector

$$q_i = -(1 - c_{4\theta}) \tau^* A_{ij}^{-1} \tau_{jk} \frac{\partial \widetilde{\theta}}{\partial x_k}, \tag{3.13}$$

https://doi.org/10.1017/jfm.2013.81 Published online by Cambridge University Press

where (bold face denotes matrix notation)

$$\boldsymbol{A}^{-1} = \frac{(c_{1\theta}^2 - \frac{1}{2}Q_1)\boldsymbol{I} - c_{1\theta}(c_S\widetilde{\boldsymbol{S}}^* + c_\Omega\widetilde{\boldsymbol{\Omega}}^*) + (c_S\widetilde{\boldsymbol{S}}^* + c_\Omega\widetilde{\boldsymbol{\Omega}}^*)^2}{c_{1\theta}(c_{1\theta}^2 - \frac{1}{2}Q_1) + \frac{1}{2}Q_2} \tag{3.14}$$

and

$$Q_1 = c_S^2\,\mathrm{tr}(\widetilde{\boldsymbol{S}}^{*2}) + c_\Omega^2\,\mathrm{tr}(\widetilde{\boldsymbol{\Omega}}^{*2}), \quad Q_2 = \tfrac{2}{3}c_S^3\,\mathrm{tr}(\widetilde{\boldsymbol{S}}^{*3}) + 2c_S c_\Omega^2\,\mathrm{tr}(\widetilde{\boldsymbol{S}}^*\widetilde{\boldsymbol{\Omega}}^{*2}), \tag{3.15}$$

and $\mathrm{tr}(\cdot)$ denotes the trace of a matrix.

From the formulation of the new EASSFM, it can be seen that the modelled subgrid scalar flux is in general not aligned with the resolved scalar gradient. In fact, it can be rewritten as a mixed model

$$q_i = -\tau^*(1-c_{4\theta})\frac{A_{kj}^{-1}\tau_{jk}}{3}\frac{\partial\widetilde{\theta}}{\partial x_i} - \tau^*(1-c_{4\theta})\left(A_{ij}^{-1}\tau_{jk} - \delta_{ik}\frac{A_{lj}^{-1}\tau_{jl}}{3}\right)\frac{\partial\widetilde{\theta}}{\partial x_k}, \tag{3.16}$$

where the first term is an eddy diffusivity term. Moreover, there is a strong influence of the SGS stresses and the A_{ij}^{-1} tensor, which involves information about both the resolved strain-rate and the resolved rotation-rate tensors.

3.2. *Extension to a rotating frame of reference*

The extension of the weak equilibrium assumption to rotating and curved boundaries has been proposed by Wallin & Johansson (2002) and Gatski & Wallin (2004). Following these studies, in a rotating frame of reference embedded with the flow, the Coriolis term modifies the advection of the normalized subgrid scalar flux,

$$\frac{\mathrm{D}\xi_i}{\mathrm{D}t} = \frac{\partial\xi_i}{\partial t} + \widetilde{u}_j\frac{\partial\xi_i}{\partial x_j} + \epsilon_{ikj}\Omega_k\xi_j. \tag{3.17}$$

We keep the Coriolis contribution to the advection term, as an approximation for the advection, which implies that the weak equilibrium assumption is assumed to be valid in the rotating frame of reference, i.e. $\partial\xi_i/\partial t + \widetilde{u}_j\partial\xi_i/\partial x_j - D_i^\xi = 0$. This is a good approximation in RANS models and corresponds to the assumption that the flow is statistically homogeneous in the rotating frame only, (see Gatski & Wallin 2004).

The production of the subgrid scalar flux is modified by the Coriolis term as

$$P_{i\theta}^{SGS} = -q_j\frac{\partial\widetilde{u}_i}{\partial x_j} - \tau_{ij}\frac{\partial\widetilde{\theta}}{\partial x_j} - \epsilon_{ikj}\Omega_k q_j. \tag{3.18}$$

The model for $\Pi_{i\theta}^{SGS} - \epsilon_{i\theta}^{SGS}$ has to be frame-invariant with respect to system rotation. A frame-invariant formulation of the model for this term and a proper description of the production term (3.17) is obtained if the normalized resolved rotation-rate tensor is substituted by the normalized effective rotation-rate tensor $\widetilde{\Omega}_{ij}^* + \tau^*\epsilon_{ikj}\Omega_k$, which is the objective form of the rotation-rate tensor, also used in the RANS context (see Gatski & Wallin 2004). Finally, the modified production and advection terms and the frame-invariant model for $\Pi_{i\theta}^{SGS} - \epsilon_{i\theta}^{SGS}$ can be accounted for by modifying $\widetilde{\Omega}_{ij}^*$ to

$$\widetilde{\Omega}_{ij}^{*R} = \widetilde{\Omega}_{ij}^* + \frac{c_\Omega + 1}{c_\Omega}\tau^*\epsilon_{ikj}\Omega_k. \tag{3.19}$$

This is the only modification needed to extend the model to rotating flows.

https://doi.org/10.1017/jfm.2013.81 Published online by Cambridge University Press

3.3. *Determination of the model parameters*

Similar to Marstorp *et al.* (2009), we derive a model for the coefficient for the return to isotropy term in (3.9), $c_{1\theta}$, using the DNS data of turbulent channel flow at $Re_\tau = 590$ (case 9 in table 2) and the return to isotropy concept. For this purpose, we write the Poisson equation for the subgrid pressure, p'', as

$$\frac{1}{\rho}\frac{\partial^2 p''}{\partial x_i \partial x_i} = -\frac{\partial^2}{\partial x_i \partial x_i}[(\widetilde{u}_i\widetilde{u}_j - \widetilde{\widetilde{u}_i\widetilde{u}_j}) + (\widetilde{u}_i u_j'' - \widetilde{\widetilde{u}_i u_j''}) + (u_i''\widetilde{u}_j - \widetilde{u_i''\widetilde{u}_j}) + (u_i'' u_j'' - \widetilde{u_i'' u_j''})], \tag{3.20}$$

where u_i'' denotes the subgrid velocity. As in RANS terminology, p'' can be divided into a rapid and a slow part, where the latter depends on subgrid quantities and the former depends on the resolved ones

$$p'' = p''_{slow} + p''_{rapid}. \tag{3.21}$$

Using this decomposition, we derive the Poisson equation for the slow pressure term from (3.20), by taking into account only those terms that involve subgrid quantities,

$$\frac{1}{\rho}\frac{\partial^2 p''_{slow}}{\partial x_i \partial x_i} = -\frac{\partial^2}{\partial x_i \partial x_j}(u_i'' u_j'' - \widetilde{u_i'' u_j''}). \tag{3.22}$$

If we solve this Poisson equation for p''_{slow}, we can compute the slow part of the subgrid pressure scalar-gradient vector,

$$\Pi_{i\theta}^{slow} = \widetilde{p''_{slow}\frac{\partial \theta''}{\partial x_i}}, \tag{3.23}$$

where θ'' is the subgrid scalar. We model $\Pi_{i\theta}^{slow}$ using the return to isotropy concept, which corresponds to the first term on the right-hand side of (3.9),

$$\Pi_{i\theta}^{slow} = -c_{1\theta} q_i \frac{\epsilon_K^{SGS}}{K^{SGS}}. \tag{3.24}$$

Using (3.23) and (3.24), we can approximate $c_{1\theta}$ as

$$c_{1\theta} = \frac{\langle |\Pi_{i\theta}^{slow}| K^{SGS} \rangle}{\langle |q_i| \epsilon_K^{SGS} \rangle}, \tag{3.25}$$

where we have taken the absolute value of the vector quantities ($|\cdot|$) and used spatial averaging over homogeneous directions ($\langle \cdot \rangle$).

Sjögren & Johansson (2000) showed that the Rotta constant in a RANS model decreases with decreasing turbulence Reynolds number. In wall-bounded flows, the local turbulence Reynolds number decreases close to the wall, and wall damping of the Rotta constant can therefore be justified. In the EASSM by Marstorp *et al.* (2009), wall damping of the model parameter c_1 analogous with the damping of the Rotta constant is applied. The consequence is that the return to isotropy becomes weaker when the wall is approached, which improves the performance of the model in shear flows. For the present EASSFM, we apply the same approach to the $c_{1\theta}$ coefficient. To model the reduced relaxation towards isotropy, $c_{1\theta}$ is described in terms of the SGS kinetic energy K^{SGS}, the filter width Δ, the norm of the filtered strain-rate

https://doi.org/10.1017/jfm.2013.81 Published online by Cambridge University Press

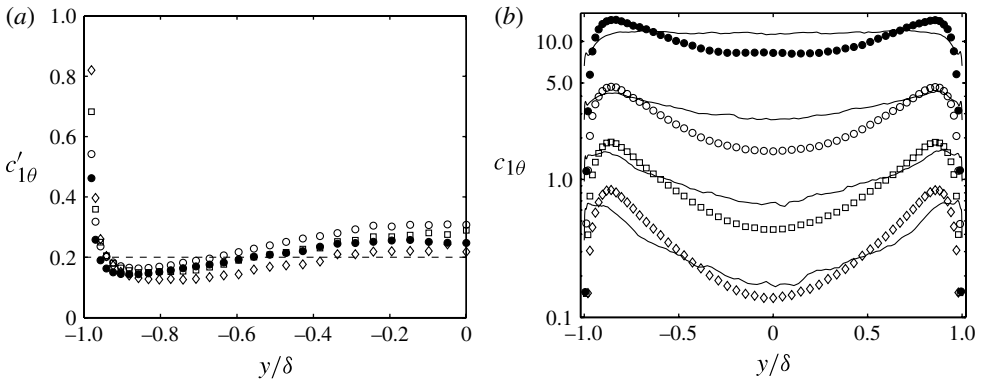


FIGURE 1. (*a*) *A priori* computed $c'_{1\theta}$ at various filter sizes (symbols) and (*b*) *a priori* computed $c_{1\theta}$ using model (3.26) at various filter sizes (symbols). The solid lines denote filtered DNS data for the corresponding filter sizes using relation (3.25). Symbols correspond to the following filter sizes in wall units: $\diamond$, $\sqrt{\Delta_x\Delta_z}^+ = 20.5$; $\square$, $\sqrt{\Delta_x\Delta_z}^+ = 28.5$; $\bigcirc$, $\sqrt{\Delta_x\Delta_z}^+ = 41.0$; $\bullet$, $\sqrt{\Delta_x\Delta_z}^+ = 82.0$.

tensor $|\widetilde{S}_{ij}| = \sqrt{2\widetilde{S}_{ij}\widetilde{S}_{ij}}$ and the time scale of the SGS scalar field $\tau_\theta = K_\theta^{SGS}/\epsilon_\theta^{SGS}$ as

$$c_{1\theta} = c'_{1\theta}\left(\frac{K^{SGS}}{(0.1\Delta|\widetilde{S}_{ij}|)^2}\right)^{\alpha_1}\left(\tau_\theta|\widetilde{S}_{ij}|\right)^{\alpha_2}, \tag{3.26}$$

where $0.1\Delta|\widetilde{S}_{ij}|$ is an eddy viscosity type of velocity scale and $\tau_\theta = Pr(K^{SGS}/\epsilon_K^{SGS})$. The model can thus account for the deviation from equilibrium of the SGS. As a result, $c_{1\theta}$ will be scale-invariant in high-Reynolds-number isotropic turbulence and will depend on the local flow properties in a case like channel flow. From *a priori* analysis, the values $\alpha_1 = 1.0$ and $\alpha_2 = 0.7$ are obtained. In order to find the value of $c'_{1\theta}$, we evaluated $c_{1\theta}$ from (3.25) and the modelled $c_{1\theta}$ from (3.26) using filtered DNS data and computed the value of $c'_{1\theta}$ *a priori*. The DNS data are again taken from simulations of turbulent channel flow at $Re_\tau = 590$ and $Pr = 0.71$ (case 9 in table 2) filtered using a sharp cutoff filter in homogeneous directions using different filter sizes. The predicted $c'_{1\theta}$ values are shown in figure 1(*a*), where the variation is fairly small with resolution and $c'_{1\theta}$ is relatively constant away from the walls. In the following simulations, we use a value of $c'_{1\theta} = 0.2$ as an approximation for this model parameter. The predicted and modelled values of $c_{1\theta}$ with $c'_{1\theta} = 0.2$ are shown in figure 1(*b*), where we can see an acceptable agreement between the modelled and reference values computed from DNS data. To avoid numerical instabilities in the simulations, it is necessary to have $c_{1\theta} \geqslant 0.5$.

Furthermore, in order to take into account the dependence on the filter size and improve the predictions, we apply a correction to $c'_{1\theta}$ in (3.26) in the form

$$c'_{1\theta}(2\Delta) = 10^{-x}c'_{1\theta}(\Delta), \quad x = 0.1(Re_{2\Delta}^{0.7} - Re_\Delta^{0.7}) - 0.3, \tag{3.27}$$

where $Re_{n\Delta} = n\Delta|\widetilde{S}_{ij}|/\nu$ is the mesh Reynolds number (Voke 1996). This correction is an analytical power-law fit, calibrated using *a priori* analysis of DNS data and is similar in formulation to the approach for computing a scale-dependent dynamic

https://doi.org/10.1017/jfm.2013.81 Published online by Cambridge University Press

coefficient for the DEVM (see e.g. Sagaut 2010). This correction improves $c_{1\theta}$ predictions at test-filter level at a filter width of 2Δ.

The model coefficient $c_{4\theta}$ can be computed using the Germano identity for the subgrid scalar flux,

$$\widehat{\widetilde{u}_i\widetilde{\theta}} - \widehat{\widetilde{u}}_i\widehat{\widetilde{\theta}} = -(1-c_{4\theta})\mathcal{T}^*\mathcal{A}_{ij}^{-1}T_{jk}\frac{\partial\widehat{\widetilde{\theta}}}{\partial x_k} + (1-c_{4\theta})\,\widehat{\tau^*A_{ij}^{-1}\tau_{jk}}\frac{\partial\widetilde{\theta}}{\partial x_k}, \tag{3.28}$$

where $\widehat{\cdot}$ denotes a test-filtered quantity with a filter width of 2Δ. The first term on the right-hand side is the modelled subtest-filter scalar flux computed from (3.13) using test-filtered quantities, $\mathcal{T}^*$ is the time scale of the subtest-filtered motions, T_{jk} is the subtest-filtered stress tensor and $\mathcal{A}_{ij}$ is the matrix A_{ij} computed using test-filtered quantities. The second term on the right-hand side is the test-filtered modelled SGS scalar flux. We denote

$$\mathcal{M}_{i\theta} = -\mathcal{T}^*\mathcal{A}_{ij}^{-1}T_{jk}\frac{\partial\widehat{\widetilde{\theta}}}{\partial x_k} + \widehat{\tau^*A_{ij}^{-1}\tau_{jk}}\frac{\partial\widetilde{\theta}}{\partial x_k}, \quad \mathcal{L}_{i\theta} = Q_i - \widehat{q}_i, \tag{3.29}$$

where Q_i is the subtest-filter scalar flux and $\widehat{q}_i$ is the test-filtered SGS scalar flux. We compute $c_{4\theta}$ using a least-squares approach,

$$c_{4\theta} = \frac{(\mathcal{M}_{i\theta}-\mathcal{L}_{i\theta})M_{i\theta}}{\mathcal{M}_{j\theta}\mathcal{M}_{j\theta}} \quad\Longrightarrow\quad 1-c_{4\theta} = \frac{\mathcal{L}_{i\theta}M_{i\theta}}{\mathcal{M}_{j\theta}\mathcal{M}_{j\theta}}. \tag{3.30}$$

We limit $c_{4\theta}$ to positive values, which means that the last term in (3.9) should not increase the production of the SGS scalar flux but always acts as a counterbalancing term. In the LESs carried out in this paper, no averaging in the homogeneous directions was necessary for smoothing of the computed $c_{4\theta}$ values. Therefore, one can use this procedure in complex geometries where there is no direction of homogeneity in the flow.

The model parameters c_Ω and c_s are introduced in the model for $\Pi_{i\theta}^{SGS} - \epsilon_{i\theta}^{SGS}$. The influence of these model parameters is similar to the $c_{4\theta}$ coefficient. Their values are not prescribed *a priori* and are found from *a posteriori* LES computations for the case of turbulent channel flow; they were found also to be reasonable values for the case of rotating channel flow. The values that we use in the simulations are $c_\Omega = 0.5$ and $c_s = 0.2$, which correspond to $c_{2\theta} = 0.65$ and $c_{3\theta} = 0.15$.

3.4. *Evaluation of the approximations* $P_K^{SGS} = \epsilon_K^{SGS}$ *and* $P_\theta^{SGS} = \epsilon_\theta^{SGS}$

The approximation $P_K^{SGS} = \epsilon_K^{SGS}$ was used by Marstorp *et al.* (2009) in the derivation of the EASSM. We also use this approximation as well as its counterpart for the SGS scalar flux, $P_\theta^{SGS} = \epsilon_\theta^{SGS}$. An *a priori* evaluation of these two approximations is given in figure 2(*a*,*b*), where we have used DNS data of turbulent channel flow with scalar transport at $Re_\tau = 590$ with $Pr = 0.71$ (case 9 in table 2). The DNS data were filtered using a sharp cutoff filter in Fourier space. Filtering was carried out in horizontal planes and was performed with various filter sizes as shown in the figures. It can be concluded that both approximations are reasonably valid especially away from the walls. However, as mentioned in Marstorp *et al.* (2009) for $P_K^{SGS} = \epsilon_K^{SGS}$, these approximations may be less valid in other types of flows, e.g. in the rotating flow cases.

https://doi.org/10.1017/jfm.2013.81 Published online by Cambridge University Press

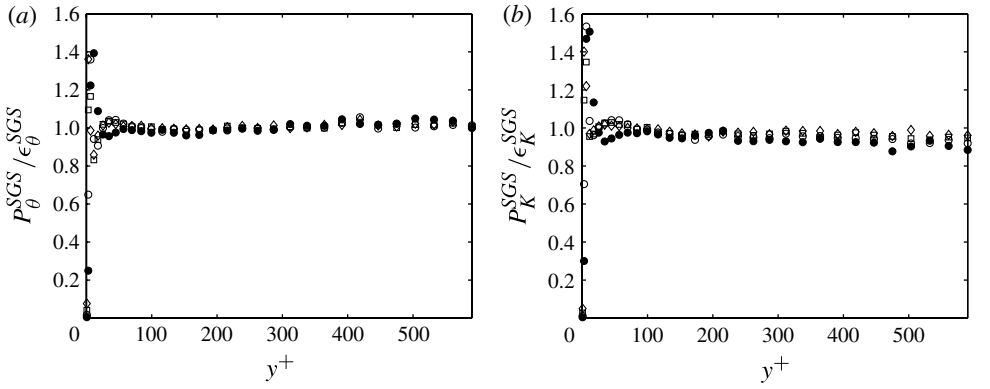


FIGURE 2. *A priori* test of (*a*) $P_\theta^{SGS}/\epsilon_\theta^{SGS}$ and (*b*) $P_K^{SGS}/\epsilon_K^{SGS}$ at various filter sizes. Different symbols correspond to different filter sizes. Filter sizes for both figures correspond to the following resolutions in wall units: ⋄, $\sqrt{\Delta_x\Delta_z}^+ = 20.5$; □, $\sqrt{\Delta_x\Delta_z}^+ = 28.5$; ○, $\sqrt{\Delta_x\Delta_z}^+ = 41.0$; ●, $\sqrt{\Delta_x\Delta_z}^+ = 82.0$.

3.5. *Evaluation of the weak equilibrium assumption*

In order to evaluate the validity of the weak equilibrium assumption for the normalized SGS scalar flux, budget terms of the normalized SGS scalar flux from (3.7) are computed from filtered DNS data at $Re_\tau = 590$ and $Pr = 0.71$ and at a typical LES resolution ($\sqrt{\Delta_x\Delta_z}^+ = 41.0$). The budget terms for the streamwise and the wall-normal components are plotted in figure 3(*a*,*b*). For the streamwise component, the production term is balanced by the dissipation and the pressure scalar-gradient correlation terms, and the weak equilibrium assumption is valid in most of the channel in the mean. For the wall-normal component, the dissipation term is small and the production term is balanced by the pressure scalar-gradient term, and the weak equilibrium assumption holds (in the time- or plane-averaged sense) only away from the wall. This means that the diffusion term plays a role very close to the wall. However, it is worth mentioning that the budget terms for the wall-normal component are much smaller than those of the streamwise component, and the error in the approximation is therefore less severe.

4. Numerical approach and SGS models

4.1. *Numerical approach*

LESs of turbulent channel flow with and without system rotation are carried out using a pseudo-spectral Navier–Stokes solver, similar to the one employed by Kim, Moin & Moser (1987). The code uses Fourier representation in wall-parallel directions (x and z), using periodic boundary conditions, and Chebyshev representation in the wall-normal direction (y), using the Chebyshev-tau method. Aliasing errors are removed using the 3/2 rule (Canuto *et al.* 1988). The time integration is carried out using a four-step third-order Runge–Kutta scheme for the nonlinear terms and a second-order Crank–Nicolson scheme for the linear terms (Lundbladh, Henningson & Johansson 2004; Chevalier *et al.* 2007). A passive scalar field (temperature) is included in the simulations. In all simulation cases, the walls are kept at constant and uniform but different temperatures, and the no-slip condition for the velocity is used at the walls.

In order to compute SGS quantities from the DNS data for comparison with the LES results, the DNS data are filtered to the corresponding LES resolution using

https://doi.org/10.1017/jfm.2013.81 Published online by Cambridge University Press

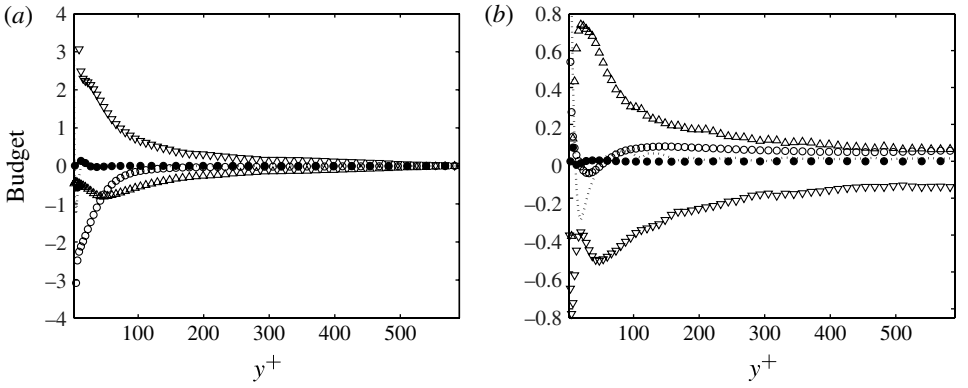


FIGURE 3. *A priori* evaluation of the budget terms of (*a*) the streamwise and (*b*) the wall-normal components of (3.7) at a filter size of $\sqrt{\Delta_x \Delta_z}^+ = 41.0$: ○, $-\epsilon_{i\theta}^{SGS}/\sqrt{k_\theta^{SGS}}K^{SGS}$; ●, $-(\xi_i/2)[(P_\theta^{SGS} - \epsilon_\theta^{SGS})/K_\theta^{SGS} + (P_K^{SGS} - \epsilon_K^{SGS})/K^{SGS}]$; △, $\Pi_{i\theta}^{SGS}/\sqrt{k_\theta^{SGS}}K^{SGS}$; ▽, $P_{i\theta}^{SGS}/\sqrt{k_\theta^{SGS}}K^{SGS}$. The negative of the sum is denoted by the dotted line.

a sharp spectral filter in the homogeneous directions. A sharp spectral filter in Chebyshev space, in the wall-normal direction, was also employed in the preliminary tests, but it is omitted here since its impact was very marginal.

4.2. *SGS stress models*

We use the EASSM by Marstorp *et al.* (2009) as the SGS stress model for the LES of turbulent channel flow using the new EASSFM. This model provides for a realistic description of the individual SGS stresses, which is advantageous since the new EASSFM depends explicitly on the SGS stresses. The EASSM consists of three terms,

$$\tau_{ij} = K^{SGS}(\tfrac{2}{3}\delta_{ij} + \beta_1 \tau^* \widetilde{S}_{ij} + \beta_4 \tau^{*2}(\widetilde{S}_{ik}\widetilde{\Omega}_{kj} - \widetilde{\Omega}_{ik}\widetilde{S}_{kj})), \tag{4.1}$$

where the first term is the isotropic part, the second term is an eddy viscosity part, and the third term is a nonlinear tensor that creates anisotropy of the SGS stresses. The coefficients β_1 and β_4 determine the relative contributions of the eddy viscosity and the nonlinear terms, and are given by

$$\beta_4 = -\frac{33}{20}\frac{1}{[(9c_1/4)^2 + |\widetilde{\Omega}_{ij}^*|^2]}, \quad \beta_1 = \frac{9}{4}c_1\beta_4, \tag{4.2}$$

where τ^* is the time scale of the SGS motions and $|\widetilde{\Omega}_{ij}^*| = \sqrt{2\widetilde{\Omega}_{ij}^*\widetilde{\Omega}_{ij}^*}$ is the norm of the normalized resolved rotation-rate tensor. The EASSM employed here uses dynamic determination of K^{SGS} as

$$K^{SGS} = c\Delta^2 |\widetilde{S}_{ij}|^2, \tag{4.3}$$

where c is dynamically determined using the Germano identity with averaging in the homogeneous directions. An alternative model for K^{SGS} suitable for LES in geometries with no direction of homogeneity, which does not require a dynamic procedure, is proposed by Marstorp *et al.* (2009). One can also use the Lagrangian dynamic

https://doi.org/10.1017/jfm.2013.81 Published online by Cambridge University Press

procedure proposed by Meneveau, Lund & Cabot (1996) to compute c or solve for a transport equation for K^{SGS} (see e.g. Ghosal *et al.* 1995). In this study, we use the dynamic procedure using the Germano identity to determine c.

The model parameter c_1 in (4.2) is determined from the dynamic coefficient c as

$$c_1 = c_1' \sqrt{c_3'} \frac{c^{1.1}}{(2C_s)^{2.5}}, \tag{4.4}$$

and the SGS time scale, τ^*, is modelled using the inverse shear

$$\tau^* = c_3' \frac{1.5C^{1.5}\sqrt{c}}{2C_s} |\widetilde{S}_{ij}|^{-1}, \tag{4.5}$$

where $c_1' = 4.2$, $c_3' = 2.4$, $C = 1.6$ is the Kolmogorov constant and $C_s = 0.1$ (see Marstorp *et al.* (2009) for details). The system rotation is accounted for in the same way as was done for the EASSFM by simply replacing $\widetilde{\Omega}_{ij}^*$ by $\widetilde{\Omega}_{ij}^{*R}$,

$$\widetilde{\Omega}_{ij}^{*R} = \widetilde{\Omega}_{ij}^* - \tfrac{25}{18}\tau^* \epsilon_{ijk}\Omega_k. \tag{4.6}$$

The other SGS stress model used for comparison is the dynamic eddy viscosity model (DEVM) of Germano *et al.* (1991), which we use together with the dynamic eddy diffusivity model (DEDM). This model has the formulation

$$\tau_{ij} - \tfrac{2}{3}\delta_{ij}K^{SGS} = -2c_{ev}\Delta^2|\widetilde{S}_{ij}|\widetilde{S}_{ij}, \tag{4.7}$$

where c_{ev} is computed dynamically using the Germano identity with modifications of Lilly (1992). Averaging of the dynamic coefficient is done in the homogeneous directions and the coefficient is clipped to positive values. The SGS kinetic energy, K^{SGS}, is not modelled and is lumped into the pressure term in (2.1).

In all LES calculations where test-filtered quantities are needed for the dynamic procedures, a sharp spectral cutoff filter at a filter width $\widehat{\Delta} = 2\Delta$ is used in the homogeneous directions.

4.3. *SGS scalar flux models*

The EASSFM, equation (3.13), is used as the SGS scalar flux model. The model coefficient $c_{1\theta}$ is computed using model (3.26) with the correction introduced in (3.27) and $c_{1\theta}' = 0.2$. The dynamic model coefficient $c_{4\theta}$ is computed using (3.30), $c_\Omega = 0.5$ and $c_s = 0.2$.

The performance of the EASSFM is compared to that of the DEDM, where the SGS scalar flux vector is modelled to be proportional to the resolved scalar gradient,

$$q_i = -\frac{\nu^{SGS}(\Delta)}{Pr^{SGS}}\frac{\partial\widetilde{\theta}}{\partial x_i}, \quad \nu^{SGS}(\Delta) = c_{ev}\Delta^2|\widetilde{S}_{ij}|, \tag{4.8}$$

where the SGS Prandtl number, Pr^{SGS}, has to be given *a priori* or computed dynamically. We use the procedure proposed by Moin *et al.* (1991) to compute Pr^{SGS} dynamically using the Germano identity,

$$Pr^{SGS} = -\frac{\mathcal{M}_{i\theta}\mathcal{M}_{i\theta}}{\mathcal{M}_{i\theta}\mathcal{L}_{i\theta}}, \tag{4.9}$$

where

$$\mathcal{M}_{i\theta} = \nu^{SGS}(2\Delta)\frac{\partial\widehat{\widetilde{\theta}}}{\partial x_i} - \widehat{\nu^{SGS}(\Delta)\frac{\partial\widetilde{\theta}}{\partial x_i}}, \quad \mathcal{L}_{i\theta} = Q_i - \widehat{q}_i, \tag{4.10}$$

https://doi.org/10.1017/jfm.2013.81 Published online by Cambridge University Press

Acronym	Subgrid stress model	Subgrid scalar flux model
EA–EA	EASSM	EASSFM
ED–EA	EASSM	DEDM
ED–EV	DEVM	DEDM

EASSM	Explicit algebraic subgrid stress model
EASSFM	Explicit algebraic subgrid scalar flux model
DEDM	Dynamic eddy diffusivity model
DEVM	Dynamic eddy vicosity model

TABLE 1. List of acronyms used in the paper.

$\widehat{\cdot}$ denotes a test-filtered quantity with a filter width 2Δ and Q_i is the subtest-filter scalar flux. Here we have used a least-squares method to determine Pr^{SGS}, which is slightly different from the approach by Moin *et al.* (1991). The dynamic coefficient c_{ev} for the computation of the SGS viscosity, ν^{SGS}, is computed using the Germano identity. The test filter is a sharp spectral filter. Averaging of c_{ev} and Pr^{SGS} in the homogeneous directions and clipping to positive values are used to stabilize the simulations.

4.4. *Combination of SGS stress and scalar flux models*

In the simulations that are presented in this paper, the EASSFM is used only in combination with the EASSM. This is due to the fact that it uses the SGS stresses in its formulation; therefore, a good description of the SGS stresses is necessary for this model. The combined EASSFM and EASSM is henceforth called the EA–EA model. The DEDM is used in combination with the EASSM, henceforth called the ED–EA model. This is a good choice for comparison with the EA–EA model, since the velocity field is the same for the two SGS scalar flux models and the two model performances can be compared directly. The DEDM is also used in combination with the DEVM, henceforth called the ED–EV model. The combination of the DEDM and the DEVM is used for further comparison, since they are based on similar concepts and are used together in practice. Table 1 summarizes the acronyms used throughout this paper.

5. Simulations of scalar transport in non-rotating channel flow

Simulation parameters for the LESs of non-rotating turbulent channel flows are given in table 2. LESs are carried out using a constant mass flux constraint with a bulk Reynolds number corresponding to that of a DNS at a friction Reynolds number $Re_\tau = 590$, based on wall shear velocity, u_τ, and channel half height, δ. Two Prandtl numbers are used, namely $Pr = 0.71$ and 1.5. In order to verify the LES results, a DNS at $Re_\tau = 590$ is carried out for these Prandtl numbers. The DNS parameters are also given in table 2 (case 9), which are similar to the DNS of Moser, Kim & Mansour (1999) without scalar transport. In all simulations, both DNS and LES, the computational domain sizes in the streamwise and spanwise directions are $L_x = 2\pi\delta$ and $L_z = \pi\delta$, respectively, where δ is the channel half height (see figure 4). To investigate the filter-scale dependence of the predicted Nusselt number, LESs are carried out at different resolutions.

https://doi.org/10.1017/jfm.2013.81 Published online by Cambridge University Press

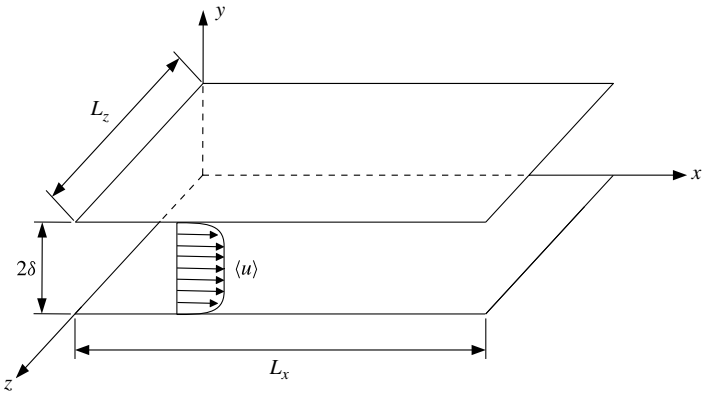


FIGURE 4. Schematic of the flow domain.

Case	SGS model	Re_τ	$N_x \times N_y \times N_z$	Δ_x^+	Δ_y^+	Δ_z^+	Nusselt number	
					min–max		$Pr = 0.71$	$Pr = 1.5$
1	EA–EA ED–EA	586	$96 \times 97 \times 96$	38.3	0.31–19.2	19.2	8.63 8.45	14.00 13.65
2	EA–EA ED–EA	592	$64 \times 65 \times 64$	58.1	0.71–28.9	29.0	8.53 8.27	13.69 13.23
3	EA–EA ED–EA	591	$32 \times 65 \times 32$	116.0	0.70–28.7	58.0	8.82 7.97	13.24 12.28
4	EA–EA ED–EA	588	$24 \times 65 \times 24$	153.8	0.71–28.8	76.9	9.23 7.87	13.45 11.96
5	ED–EV	581	$96 \times 97 \times 96$	38.0	0.31–19.0	19.0	8.65	14.11
6		570	$64 \times 65 \times 64$	56.0	0.68–27.8	28.0	8.23	13.53
7		537	$32 \times 65 \times 32$	105.4	0.64–26.1	52.7	7.41	11.82
8		517	$24 \times 65 \times 24$	135.4	0.62–25.3	67.7	6.92	10.88
9	—	590	$384 \times 257 \times 384$	9.6	0.04–7.2	4.8	8.76	14.34

TABLE 2. Summary of simulations for non-rotating turbulent channel flow. See table 1 for a list of acronyms. Here N_x and N_z are the number of Fourier modes in streamwise and spanwise directions, respectively, excluding the de-aliasing modes; and N_y denotes the number of Chebyshev polynomials in the wall–normal direction.

5.1. *Mean velocity and Reynolds stresses*

Figure 5(*a*,*b*) show LES and DNS results of the mean velocity profile and the Reynolds stresses predicted by the EASSM and the DEVM corresponding to cases 2 and 6 (LES) and case 9 (DNS). To make a fair comparison between LES results and DNS data, Winckelmans, Jeanmart & Carati (2002) suggest adding the contribution from the modelled part to the resolved statistics. However, it is not possible to do this for the Reynolds stresses for the DEVM, since the modelled SGS kinetic energy is lumped in the pressure term in the Navier–Stokes equations, see (4.7), and therefore

https://doi.org/10.1017/jfm.2013.81 Published online by Cambridge University Press

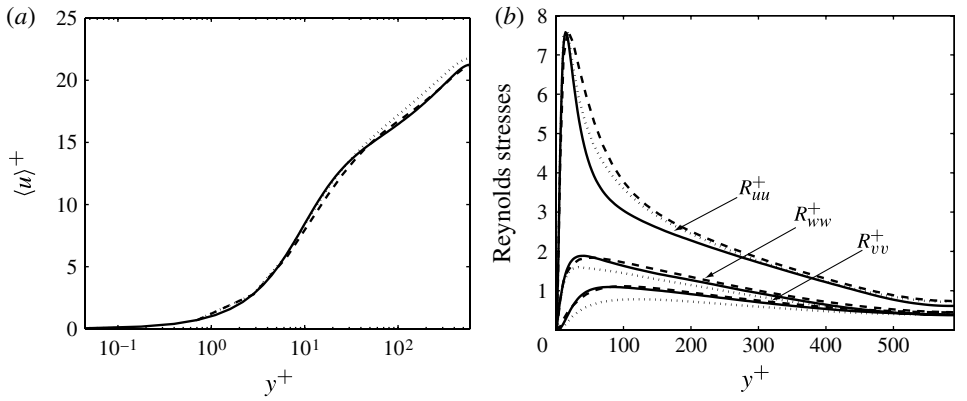


FIGURE 5. (*a*) Mean velocity profiles and (*b*) resolved plus modelled (the modelled part is added only for the EASSM) normal Reynolds stresses (R_{uu}, R_{vv} and R_{ww}) in wall units. DNS data, solid line; EASSM, dashed line; DEVM, dotted line.

the modelled part is not added to the resolved one. However, for the EASSM, the modelled part is available and is added to the resolved stresses. Since in the DEVM only the resolved normal stresses are available while in the EASSM both the resolved and SGS normal stresses are available, a direct quantitative comparison between their predictions for the total Reynolds stresses is not appropriate.

Figure 5(*a*) shows a good agreement between LES and DNS results for the mean velocity profile. There is a slight over-prediction by the DEVM in the mean velocity profile in the logarithmic region, indicating that the wall shear stress is under-predicted. The EASSM prediction is close to the DNS profile, showing that the model correctly predicts the wall shear stress. This can also be verified by looking at the Re_τ predictions of the two models in table 2, which indicates that the DEVM under-predicts the wall shear stress by 6.7 % whereas the EASSM prediction is accurate.

At this resolution, the EASSM predicts the streamwise, R_{uu}, the wall-normal, R_{vv}, and the spanwise, R_{ww}, Reynolds stresses in good agreement with the DNS data. A direct comparison between the DEVM and the EASSM for the Reynolds stresses cannot be performed for the reasons already discussed. However, it is worth mentioning that the resolved streamwise Reynolds stress predicted by the DEVM is close to the total R_{uu} predicted by the DNS. This implies that the total streamwise Reynolds stress would be over-predicted by the DEVM, depending on the magnitude of the unknown SGS stress.

LES results at other resolutions are not presented here. In Rasam *et al.* (2011*a*,*b*), we showed that the EASSM gives good predictions at much coarser resolutions and higher Re_τ, whereas the DEVM gives poor predictions at coarser resolutions, implying that it forms a poor basis for scalar and mass transport predictions.

5.2. *Mean and root-mean-square profiles of the scalar*

The mean scalar profiles are shown in figure 6(*a*) for Prandtl numbers $Pr = 0.71$ and 1.5, where DNS (case 9) and LES (cases 2 and 6) results are compared. The scalar profiles show a linear trend as $\langle\theta\rangle^+ = y^+Pr$ for $y^+ < 5.0$, corresponding to the diffusive sublayer, and have a logarithmic behaviour for $y^+Pr > 30$–50 (Bradshaw &

https://doi.org/10.1017/jfm.2013.81 Published online by Cambridge University Press

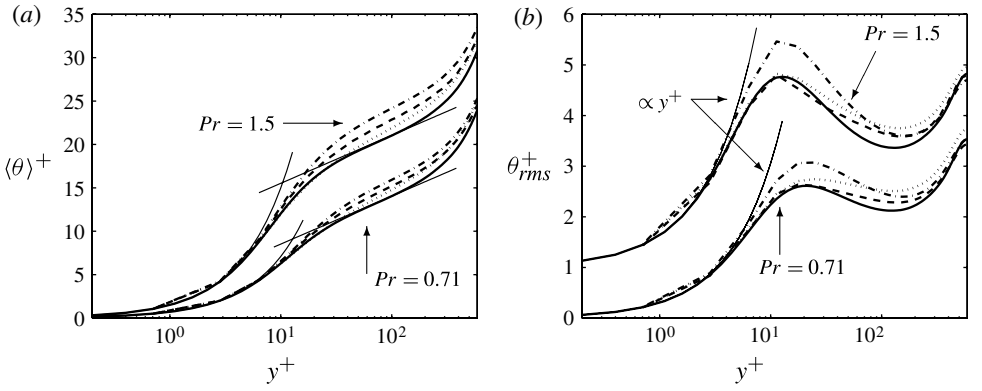


FIGURE 6. (*a*) Mean temperature, $\langle\theta\rangle^+$, and (*b*) root-mean-square of the temperature, θ^+_{rms}, normalized with $(\nu/u_\tau Pr)|\partial\langle\theta\rangle/\partial y|_{wall}$. DNS data, solid line; EA–EA model, dashed line; ED–EA model, dash-dotted line; ED–EV model, dotted line. Thin solid lines in panel (*a*): linear profile $\langle\theta\rangle^+ = y^+Pr$ and logarithmic law $\langle\theta\rangle^+ = (1/\kappa_T)\ln y^+ + B_T$. Thin solid lines in panel (*b*): linear profile of y^+. The θ^+_{rms} profiles for $Pr = 1.5$ are shifted in the ordinate direction by one wall unit for clarity of the plot.

Huang 1995), which can be described as (Kader & Yaglom 1972)

$$\langle\theta\rangle^+ = \frac{1}{\kappa_T}\ln y^+ + B_T, \tag{5.1}$$

where κ_T is the von Kármán constant for the passive scalar. The corresponding value that best fits the DNS data is $\kappa_T \approx 0.40$, which is higher than $\kappa_T \approx 0.33$ reported by Johansson & Wikström (1999) for scalar transport in a channel similar to the one used here but at a lower Reynolds number ($Re_\tau = 265$). The value of the B_T coefficient depends on the Prandtl number and its values for the best fit to the DNS data are $B_T = 2.4$ and 9.3 for $Pr = 0.71$ and 1.5, respectively. Evidently, the near-wall conduction-dominated region decreases, as the Prandtl number increases, resulting in faster mixing, which clearly sharpens the near-wall gradient of the scalar.

The root-mean-square (r.m.s.) profiles of the scalar are shown in figure 6(*b*), where the predictions at the two Prandtl numbers are separated by a shift in the ordinate direction. It can be seen from the DNS predictions that, as the Prandtl number increases, the near-wall peak moves closer to the wall and the r.m.s. increases, indicating an increase in the scalar fluctuations. The r.m.s. profiles also show a linear scaling with y^+ in the near-wall region (see also Kawamura *et al.* 1998). The r.m.s. profile has two peaks. The near-wall peak is the location of the maximum production of scalar intensity. The peak at the centre of the channel is due to the fact that the hot and cold packets of fluid that come from the walls collect around the centreline (Debusschere & Rutland 2004). Moreover, there is a non-zero production of scalar intensity at the centre of the channel due to the gradient in the mean scalar profile. The peak at the centre does not appear in channel flows with iso-flux boundary conditions, leading to symmetric scalar profiles and a minima in the r.m.s. profile at the centre of the channel.

All the LES models over-predict the mean scalar profile in comparison to the DNS for the two Prandtl numbers. If we compare the EA–EA model predictions with those of the ED–EA model, where both scalar flux models are used with the same SGS

https://doi.org/10.1017/jfm.2013.81 Published online by Cambridge University Press

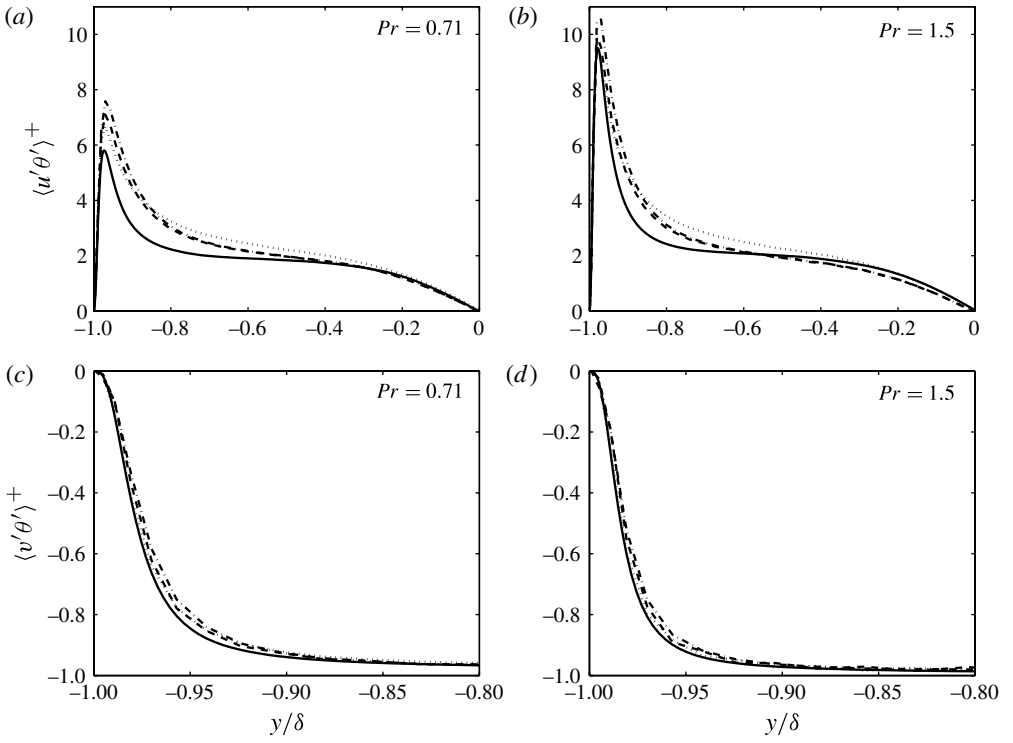


FIGURE 7. Resolved plus modelled turbulence scalar fluxes, normalized with $(\nu/Pr)|\partial\langle\theta\rangle/\partial y|_{wall}$, for Prandtl numbers $Pr = 0.71$ and 1.5: (a,b) streamwise scalar flux, $\langle u'\theta'\rangle^+$; and ($c$,$d$) wall-normal scalar flux, $\langle v'\theta'\rangle^+$. DNS data, solid line; EA–EA model, dashed line; ED–EA model, dash-dotted line; ED–EV model, dotted line.

stress model, the EA–EA model gives a better prediction for both Prandtl numbers. This is a reasonable comparison, since it ensures that the same velocity field is used for the passive scalar transport. The same comparison also holds for θ_{rms}, where the EA–EA model performs better than the ED–EA model; see figure 6(b).

Another comparison is made between the EA–EA model and the ED–EV model, where different SGS stress models are used, and therefore the velocity fields are differently predicted. Both models give similar predictions for the mean scalar profile for $Pr = 0.71$, while the ED–EV model gives better results for the mean scalar profile for $Pr = 1.5$. In both cases, the slope of the mean scalar profile in the logarithmic region is better predicted by the EA–EA model than the ED–EV model. The latter predicts a steeper mean scalar profile than that of the DNS, which shows that the molecular dissipation is over-predicted by this model, while the other model predictions of the slope of the mean scalar profile are closer to the DNS data. The two models predict the same trend as the DNS for θ_{rms}, but the EA–EA model predictions are closer to the DNS at both Prandtl numbers. The LES predictions also show a linear scaling with y^+ in the near-wall region for all models.

5.3. *Resolved scalar fluxes*

The components of the mean turbulent scalar flux vector are shown in figure 7(a–d). Once again, to make a better comparison between the LES and the DNS data, we have

https://doi.org/10.1017/jfm.2013.81 Published online by Cambridge University Press

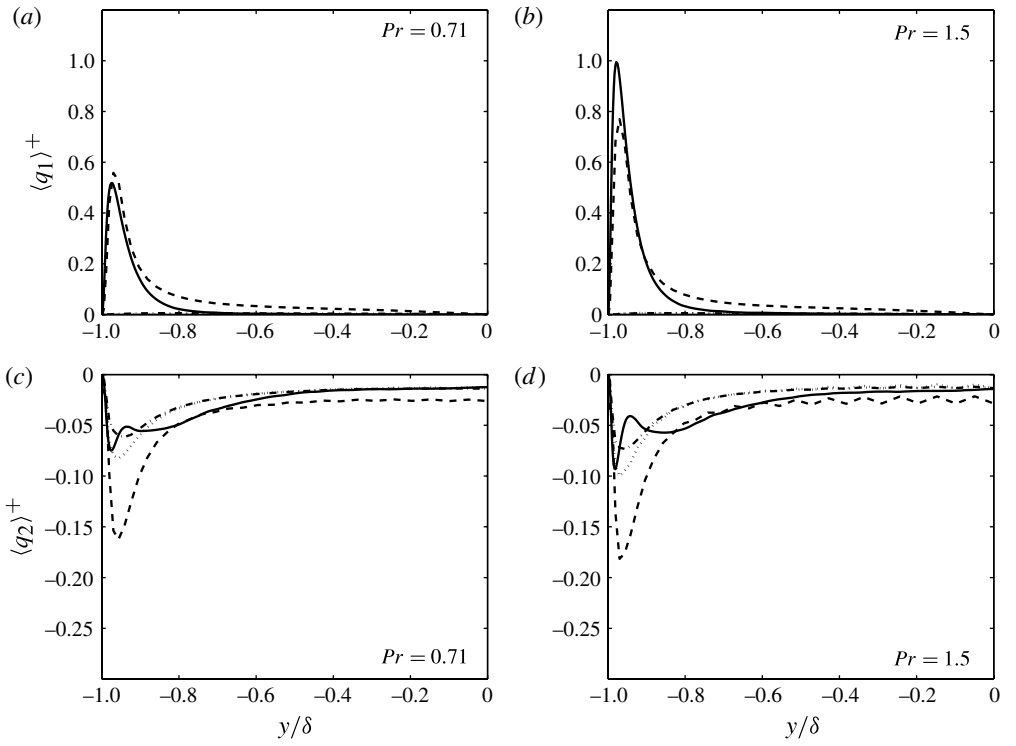


FIGURE 8. Mean SGS scalar fluxes, normalized with $(\nu/Pr)|\partial\langle\theta\rangle/\partial y|_{wall}$, for Prandtl numbers $Pr = 0.71$ and 1.5: (*a*,*b*) streamwise component, $\langle q_1\rangle^+$; and (*c*,*d*) wall-normal component, $\langle q_2\rangle^+$. Filtered DNS, solid line; EA–EA model, dashed line; ED–EA model, dash-dotted line; ED–EV model, dotted line.

added the modelled subgrid scalar fluxes to the resolved ones, similar to the Reynolds stresses. At this resolution (cases 2 and 6), model predictions are similar and in good agreement with the DNS data (case 9) for all models. The relatively small differences between model predictions shows that most scales are well resolved by the grid.

The increase in the near-wall mean scalar gradient with increasing Prandtl number (see figure 6*a*) results in an increase in the production of the resolved scalar fluxes in the near-wall region. This is consistent with the DNS data showing an increase in the peak value of $\langle u'\theta'\rangle$. The peak moves closer to the wall due to shrinking of the conduction region with increasing Prandtl number. This behaviour is also well represented by all SGS models. It is noted that the EA–EA model prediction is more accurate with increasing Prandtl number.

The wall-normal component of the scalar flux, $\langle v'\theta'\rangle$, is also similar and well predicted by all models; see figure 7(*c*,*d*). The DNS results show that $\langle v'\theta'\rangle^+$ approaches -1.0 faster with increasing Prandtl number. This indicates that the near-wall scalar transport mechanism becomes more dominated by the turbulent scalar flux as the Prandtl number increases.

5.4. *SGS scalar fluxes*

Figure 8(*a–d*) show the mean streamwise and wall-normal SGS scalar fluxes $\langle q_1\rangle$ and $\langle q_2\rangle$ for two Prandtl numbers obtained from LES (cases 2 and 6) and filtered

https://doi.org/10.1017/jfm.2013.81 Published online by Cambridge University Press

DNS data (case 9). As was pointed out in connection with figure 3(*a*), the production term in the transport equation of q_1 is much larger than that of q_2, hence the former is expected to be larger than the latter. The production of q_1 is mainly due to the interaction between SGS stresses and the resolved scalar gradient; see (3.2). In the DEDM formulation, this component of the SGS flux cannot be predicted. However, the filtered DNS data show a considerable streamwise SGS scalar flux close to the wall; see figure 8(*a*,*b*).

In general, this component is unpredictable by simple eddy diffusivity-type models that enforce alignment of the SGS flux and the resolved scalar gradient vectors. In contrast, the new model gives a good description of $\langle q_1 \rangle$ for the two Prandtl numbers. This is directly related to the use of the SGS stress tensor in its formulation. The DNS predictions show that the near-wall peak of $\langle q_1 \rangle$ increases by a factor of two with increasing Prandtl number in the diffusive sublayer, which is also predicted by the EASSFM. This is due to the fact that the near-wall scalar behaves linearly with the wall distance as $\langle \theta \rangle^+ = y^+ Pr$. Therefore its wall-normal gradient scales with Prandtl number in the diffusive sublayer. Hence, the increase in the production of $\langle q_1 \rangle$ scales roughly with the Prandtl number; see (3.2). Similar to the behaviour of $\langle u'\theta' \rangle$, the peak of $\langle q_1 \rangle$ gets closer to the wall with increasing Prandtl number, which is well predicted by the EASSFM.

As is expected, $\langle q_2 \rangle$ is relatively small compared to $\langle q_1 \rangle$, see figure 8(*c*,*d*), which makes it harder to predict. The EA–EA model over-predicts $\langle q_2 \rangle$, while the ED–EV and ED–EA models under-predict it in some parts of the channel for both Prandtl numbers. An under-prediction of $\langle q_2 \rangle$ by the DEDM leads to an under-prediction of the SGS scalar dissipation ($= -\langle q_i \partial\widetilde{\theta}/\partial x_i \rangle$) resulting in an increase in θ_{rms}. This is clearly seen in the predictions of the near-wall peak of θ_{rms} by the DEDM in figure 6(*b*). Determination of the source of the over-prediction of q_2 by the EA–EA model is not easy, as it can be related to the prediction of the SGS stresses. Another point is the influence of q_2 on the SGS dissipation. Since the modelled SGS flux is not instantly aligned with the true SGS flux, the SGS dissipation is under-predicted if q_2 is close to or smaller than the DNS value. Therefore, the over-prediction of q_2 improves the overall performance of the SGS model. Contrary to $\langle q_1 \rangle$, $\langle q_2 \rangle$ does not increase considerably with increasing Prandtl number in the DNS, but its peak moves closer to the wall with increasing Prandtl number, similar to the behaviour of $\langle v'\theta' \rangle$. The EASSFM predictions show a similar behaviour as those of the DNS.

5.5. *Anisotropy of the SGS scalar dissipation*

The properties of the SGS scalar dissipation are important for LES of scalar mixing. In contrast to the SGS dissipation of kinetic energy, the anisotropy of the SGS dissipation of scalar variance is known to persist down to very small filter scales (see Kang & Meneveau 2001). Similar to Kang and Meneveau, we define the anisotropy measure

$$I_\theta = \frac{\left\langle q_1 \dfrac{\partial\widetilde{\theta}}{\partial x} \right\rangle}{\left\langle q_2 \dfrac{\partial\widetilde{\theta}}{\partial y} \right\rangle}, \tag{5.2}$$

which is equal to unity in the case of isotropy. The anisotropy ratios I_θ resulting from LES (cases 2 and 6) and filtered DNS (case 9) are shown in figure 9 for $Pr = 0.71$. The predictions for $Pr = 1.5$ are similar and are not presented. The anisotropy plot

https://doi.org/10.1017/jfm.2013.81 Published online by Cambridge University Press

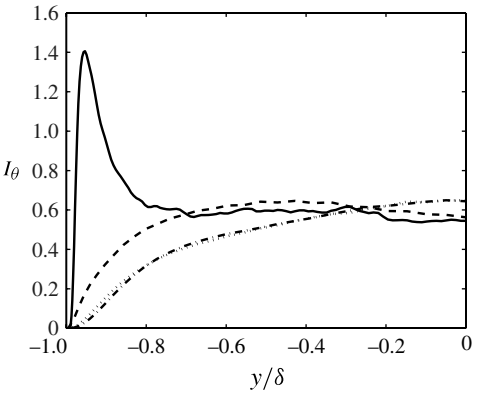


FIGURE 9. Anisotropy of the SGS scalar dissipation, I_θ, for $Pr = 0.71$. Filtered DNS, solid line; EA–EA model, dashed line; ED–EA model, dash-dotted line; ED–EV model, dotted line.

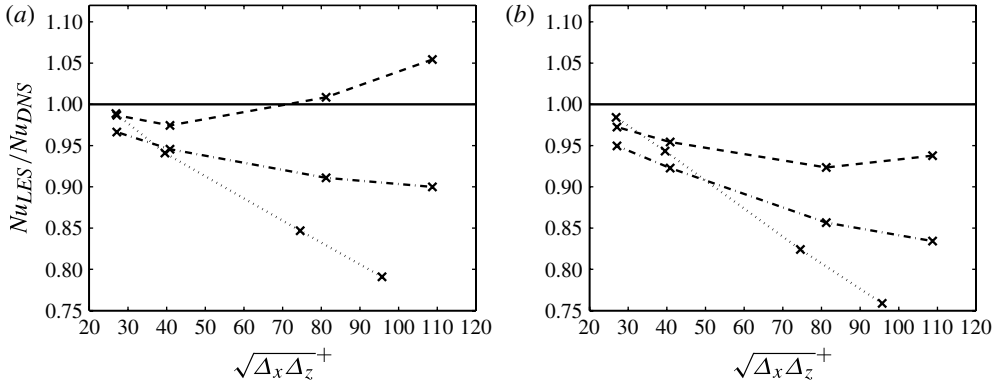


FIGURE 10. Variation of the Nusselt number of LES, Nu_{LES}, with respect to the corresponding DNS value, Nu_{DNS}, for various resolutions: (*a*) $Pr = 0.71$; (*b*) $Pr = 1.5$. DNS, solid line; EA–EA model, dashed line; ED–EA model, dash-dotted line; ED–EV model, dotted line.

from the DNS has a peak close to the wall, indicating that the streamwise component of dissipation, $\langle q_1 \partial\widetilde{\theta}/\partial x\rangle$, is 40 % larger than its wall-normal component, $\langle q_2 \partial\widetilde{\theta}/\partial y\rangle$. It also drops rapidly closer to the wall, showing that the streamwise component decreases faster than the wall-normal one as the wall is approached. In the core region of the channel, the contribution from the wall-normal component is larger with $I_\theta \approx 0.6$. Both ED–EA and ED–EV models predict a too small anisotropy close to the wall, while the EA–EA model provides for an improved description of the spatial variation of I_θ. Although it also under-predicts I_θ near the wall, the improvements are appreciable and its predictions are much closer to the DNS results than those of the other models.

5.6. *Nusselt number*

The accuracy of LES predictions of the Nusselt number is important in heat transfer applications, since it determines the heat transfer to the surface from the fluid. Figure 10(*a*,*b*) show the predicted Nusselt numbers for LES divided by those of

https://doi.org/10.1017/jfm.2013.81 Published online by Cambridge University Press

the DNS for both Prandtl numbers for various resolutions (cases 1–8). It is desirable that LES predictions follow those of the DNS for the prediction of the Nusselt number for various Prandtl numbers even at coarse resolutions. But, as will be shown later, as the resolution decreases and the model contribution increases, errors due to model parametrization grow. At coarser resolutions, the effect of anisotropic scales at the SGS level start to become significant. Therefore, it is expected that simple models like the DEDM fail to give good predictions at those resolutions, while models like the EASSFM that can represent the SGS anisotropy properly perform better.

Indeed, the EA–EA model predictions show the least variation in the prediction of the Nusselt number with changing resolution. Its predictions are also most accurate at various resolutions. The ED–EV model shows the largest dependence on the resolution, which is partly due to the sensitivity of the DEVM to resolution in prediction of velocity statistics. Its predictions are less accurate at coarser resolutions than the other models. The predictions of the ED–EA model lie in between those of the other two models. The predictions of the ED–EA model in comparison with the ED–EV model show that a better prediction of the SGS stresses decreases the dependence of the scalar predictions on the resolution. In conclusion, the new EA–EA model predictions are more reliable in a wide range of grid resolutions, which is a desirable property of this model. The smaller dependence of the accuracy of the EASSFM predictions of the Nusselt number on the grid resolution in comparison with those of the DEDM is similar to the smaller dependence of the accuracy of the EASSM predictions of the wall friction on the grid resolution in comparison with those of the DEVM presented in Rasam *et al.* (2011*a*).

6. Model assessment using the SGS activity parameter

The main role of an SGS model is to properly remove energy from the resolved scales (Meneveau 1994). Analysis of the energy extraction by the SGS model from the resolved scales can be better understood by looking at the role of different terms in the governing equation for the resolved scalar intensity, $K_\theta = \widetilde{\theta}^2/2$, which can be written in non-dimensional form as (Jiménez *et al.* 2001*b*)

$$\underbrace{\frac{\partial K_\theta}{\partial t} + \widetilde{u}_j \frac{\partial}{\partial x_j}(K_\theta)}_{\textit{advection}} = \underbrace{\frac{1}{Pe}\frac{\partial^2 K_\theta}{\partial x_j \partial x_j}}_{\substack{\textit{molecular}\\ \textit{diffusion}}} - \underbrace{\frac{1}{Pe}\frac{\partial \widetilde{\theta}}{\partial x_j}\frac{\partial \widetilde{\theta}}{\partial x_j}}_{\substack{\textit{molecular}\\ \textit{dissipation}}} - \underbrace{\frac{\partial}{\partial x_j}(\widetilde{\theta} q_j)}_{\substack{\textit{SGS}\\ \textit{diffusion}}} + \underbrace{q_j \frac{\partial \widetilde{\theta}}{\partial x_j}}_{\substack{\textit{SGS}\\ \textit{dissipation}}}, \tag{6.1}$$

where $Pe = Re\,Pr$ is the Péclet number. In this equation, the second term on the right-hand side represents the molecular dissipation, ϵ_α, acting on the resolved scalar intensity, while the last term is the SGS dissipation, ϵ_θ^{SGS}, which transfers energy to the subgrid motions and acts as a source term in the corresponding equation for the SGS scalar variance. The role of the diffusion term is a local transfer of K_θ, but it does not add or remove energy in a volume-averaged sense. In order to further analyse the performance of the new SGS model at various resolutions, we follow the approach by Geurts & Fröhlich (2002). They introduced an SGS activity parameter, s, defined as

$$s = \frac{\langle \epsilon_K^{SGS} \rangle}{\langle \epsilon_K^{SGS} \rangle + \langle \epsilon_\mu \rangle}, \tag{6.2}$$

for assessment of the accuracy of LES predictions. In this relation, ϵ_K^{SGS} is the SGS dissipation of the kinetic energy and ϵ_μ is the viscous dissipation. Therefore, the

https://doi.org/10.1017/jfm.2013.81 Published online by Cambridge University Press

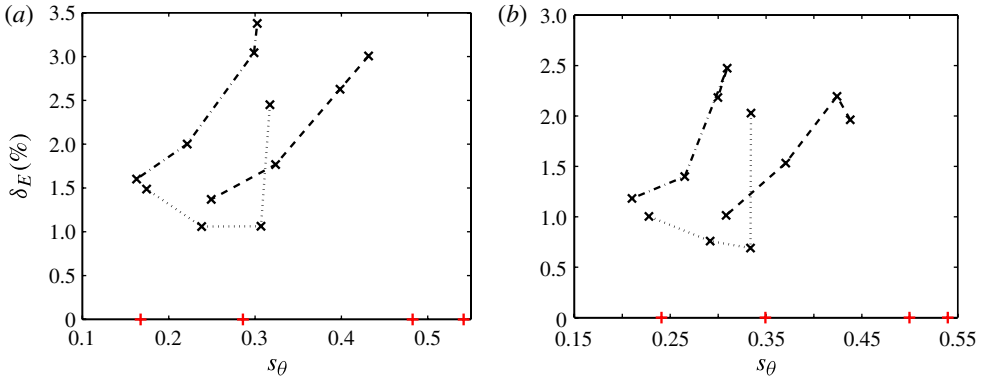


FIGURE 11. (Colour online) Normalized error, δ_E, of the time-averaged resolved scalar intensity, K_θ (integrated over the whole channel), with respect to the corresponding filtered DNS value, plotted against the SGS activity parameter, s_θ, for various resolutions: (*a*) $Pr = 0.71$; (*b*) $Pr = 1.5$. EA–EA model, dashed line; ED–EA model, dash-dotted line; ED–EV model, dotted line. The s_θ values computed from DNS data are shown with plus symbols on the abscissa.

activity parameter is the ratio between the SGS and total dissipation. In Rasam *et al.* (2011*a*), we used the SGS activity parameter to compare the accuracy of different SGS models, including the EASSM, in predicting the volume-averaged resolved kinetic energy

$$E_K = \frac{1}{|\Omega|}\int_\Omega \frac{1}{2}\widetilde{u}_i\widetilde{u}_i \,\mathrm{d}\boldsymbol{x}, \tag{6.3}$$

where Ω denotes the domain size. We extend this approach and define the SGS activity parameter s_θ for the scalar field,

$$s_\theta = \frac{\langle \epsilon_\theta^{SGS}\rangle}{\langle \epsilon_\theta^{SGS}\rangle + \langle \epsilon_\alpha\rangle}, \tag{6.4}$$

and evaluate the accuracy of LES predictions using the EASSFM for the prediction of the volume-averaged scalar intensity,

$$E_\theta = \frac{1}{|\Omega|}\int_\Omega K_\theta \,\mathrm{d}\boldsymbol{x}. \tag{6.5}$$

A small value of the SGS activity parameter, s_θ or s, indicates a well-resolved LES, with the SGS model contribution going towards zero. As the resolution decreases, it is expected that the SGS activity parameter increases, indicating an increase in the SGS model contribution.

Therefore, a proper SGS model should have a higher SGS activity parameter at coarser resolutions. Owing to parametrization errors, any SGS model prediction will have a larger error at coarser resolutions, but it is essential that, when the resolution increases, the SGS activity parameter decreases, and the error in its prediction also decreases when more scales are resolved and the subgrid scales are better modelled.

The prediction error of the scalar intensity relative to the corresponding DNS value, $\delta_E = |E_\theta^{LES} - E_\theta^{DNS}|/E_\theta^{DNS}$, as a function of s_θ is shown in figure 11(*a*,*b*) for two Prandtl numbers and four resolutions. The SGS activity parameters computed from the filtered

https://doi.org/10.1017/jfm.2013.81 Published online by Cambridge University Press

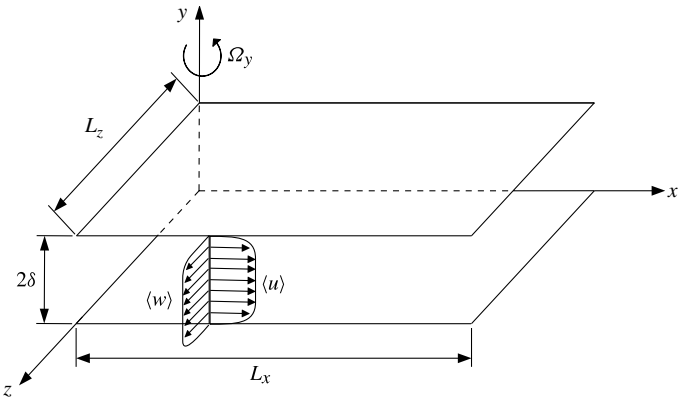


FIGURE 12. Schematic of the flow domain for the channel flow with wall-normal rotation.

DNS data are also shown in the figure. In comparison with the ED–EA model, the EA–EA model has a larger activity parameter at all resolutions and yet it has a smaller error in its predictions. Its SGS activity parameter is closer to the DNS value at coarser resolutions compared to the other models. The prediction error of the new model decreases monotonically as the resolution increases and the SGS activity goes down. It is also clear that the new model is more accurate than the ED–EA model. The behaviour of the new model is desirable since it shows a monotonic behaviour for δ_E and its predictions are relatively accurate. In contrast, the ED–EV model shows a non-monotonic behaviour. Its prediction is more accurate at moderate resolutions than the other models but becomes less accurate at the finest resolution where the SGS activity is smaller, showing that model errors grow although more scales are resolved. It also shows a sudden increase of the prediction error at the coarsest resolution, which is partly due to errors stemming from the SGS stress model. Finally, it is worth mentioning that the EASSFM's behaviour in predicting the resolved scalar intensity presented here is similar to that of the EASSM in predicting the resolved kinetic energy reported in Rasam *et al.* (2011*a*).

7. Simulations of scalar transport in channel flow with wall-normal rotation

We carry out LESs and DNSs of scalar transport in turbulent channel flow in a rotating frame of reference. The friction Reynolds number $Re_\tau = u_\tau \delta/\nu$, based on the corresponding non-rotating channel flow, is 180. The rotation vector is in the wall-normal direction and the simulations are carried out at two rotation rates, $Ro_\tau = 2\Omega_y \delta/u_\tau = 0.018$ and 0.054. The DNSs are similar to those reported by Mehdizadeh & Oberlack (2010), where they have investigated this flow case in detail for laminar and turbulent channel flow. They showed that rotation creates an Ekman-like phenomenon and deflects the mean velocity towards the spanwise direction. We extend their DNSs with passive scalar transport. The scalar considered is temperature. The channel walls are kept at constant but different temperatures and the simulations are carried out at $Pr = 0.71$. Details of the simulation parameters are given in table 3. In all simulations, both DNS and LES, the computational domain size in the streamwise and spanwise directions are $L_x = 4\pi\delta$ and $L_z = 6\pi\delta$, respectively, where δ is the channel half height (see figure 12). This flow is particularly challenging for LES, since the Coriolis force creates a shear-induced mass flux and consequently

https://doi.org/10.1017/jfm.2013.81 Published online by Cambridge University Press

Case	SGS model	Ro_τ	Re_b	$N_x \times N_y \times N_z$	Δ_x^+	Δ_y^+ min–max	Δ_z^+	Nusselt number
1	EA–EA	0.018	5405.8	48 × 49 × 96	47.12	0.38–11.8	35.3	2.89
	ED–EA							2.71
2	EA–EA	0.054	4497.3					2.48
	ED–EA							2.33
3	ED–EV	0.018	5730.0	48 × 49 × 96	47.12	0.38–11.8	35.3	2.75
4		0.054	4655.0					2.35
5	—	0.018	5487.6	128×129×384	17.67	0.054–4.42	8.83	3.00
6		0.054	4596.1					2.59

TABLE 3. Summary of simulations of turbulent channel flow with wall-normal rotation. See table 1 for the list of acronyms. Here $Re_b = u_b\delta/\nu$ is the bulk Reynolds number, where $u_b = \sqrt{u_{bx}^2 + u_{bz}^2}$ is the effective mean bulk velocity; and u_{bx} and u_{bz} are the streamwise and spanwise mean bulk velocities, respectively.

a scalar transport in the spanwise direction. This is true even for small rotation rates (Wu & Kasagi 2004). Owing to this effect, all the resolved and SGS stresses and scalar fluxes become non-zero. The only investigation of scalar transport in the case of channel flow with wall-normal rotation is carried out by Li & Liu (2006), who have performed DNSs of channel flow at $Re_\tau = 194$ with $Pr = 1.0$ for rotation numbers between 0.0 and 0.1. As was pointed out by Mehdizadeh & Oberlack (2010), at sufficiently high rotation rates a quasi-laminar state develops. In the simulations presented here, the rotation rates are small and the flow is fully turbulent.

7.1. *Near-wall turbulent structures*

The rotational effects on the flow physics can be illustrated by flow visualizations. Figure 13(*a–l*) demonstrate snapshots of the instantaneous streamwise and spanwise velocities as well as scalar fluctuations at a near-wall plane at $y^+ \approx 15$. The second and first rows compare DNS results from the rotating turbulent channel flow at rotation number $Ro_\tau = 0.054$ (case 6 in table 3) with that of the corresponding non-rotating turbulent channel flow with identical resolutions, respectively. In the non-rotating case, the streamwise velocity fluctuations u' show streaky structures, indicating low- and high-speed streaks aligned with the mean flow, which are typical characteristics of wall-bounded flows; see figure 13(*a*). The scalar fluctuations θ' also depict streaky structures similar to those of u' (see figure 13*i*), since the scalar fluctuations are passively advected by the flow, showing that the mixing of the scalar in the near-wall region is strongly connected with the flow dynamics. Abe & Antonia (2009) showed that, in a non-rotating channel flow, the strongest similarity between u' and θ' is found near the location corresponding to the centroid of the momentum streaks ($y^+ \approx 7$), below which the similarity is weaker. The spanwise velocity fluctuations w' do not show the same characteristics as u' and θ' and only spots of high- and low-intensity fluctuations are observed (see figure 13*e*), which are due to the splatting effect (Moin & Kim 1982).

As rotation is introduced, flow structures become tilted in the spanwise direction, due to the Coriolis force. The streamwise velocity fluctuations become less intense but the streaky structures become more elongated; see figure 13(*b*). The streak spacing

https://doi.org/10.1017/jfm.2013.81 Published online by Cambridge University Press

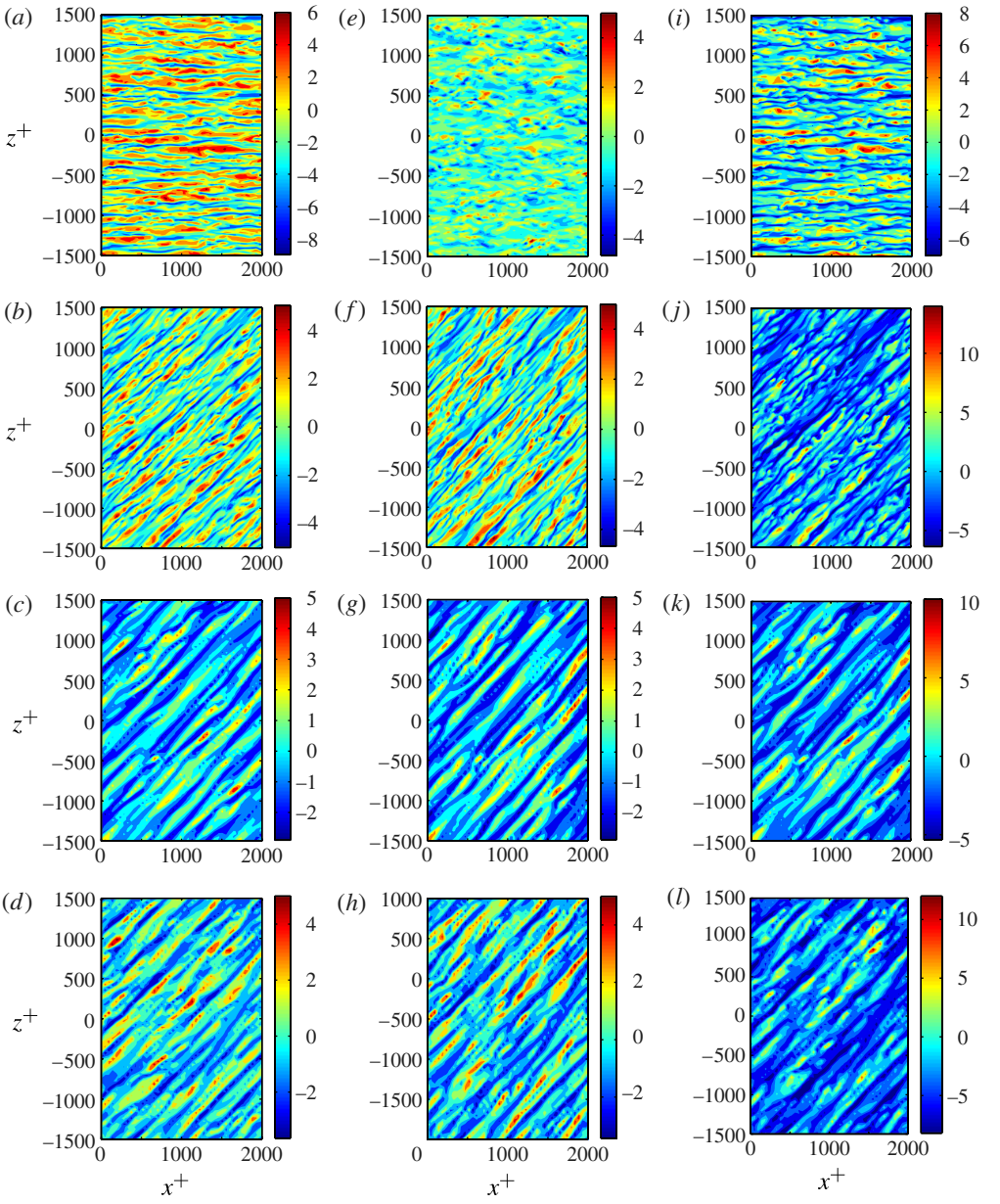


FIGURE 13. Horizontal snapshots of (*a–d*) streamwise velocity fluctuations u'^+, (*e–h*) spanwise velocity fluctuations w'^+, and (*i–l*) scalar fluctuations θ'^+ in wall units at $y^+ \approx 15$. The first and second rows are the DNS results of the non-rotating and rotating channel ($Ro_\tau = 0.054$), respectively. The third and fourth rows are LES results of the EA–EA and ED–EV models, respectively.

also increases by the introduction of the rotation (see Li & Liu 2006). The spanwise velocity and the scalar fluctuations also show streaky structures in the rotating flow case, which are tilted in the same direction as those of the streamwise fluctuations; see figure 13(*f*,*j*). The scalar fluctuations increase but it is clear from the figure that the

https://doi.org/10.1017/jfm.2013.81 Published online by Cambridge University Press

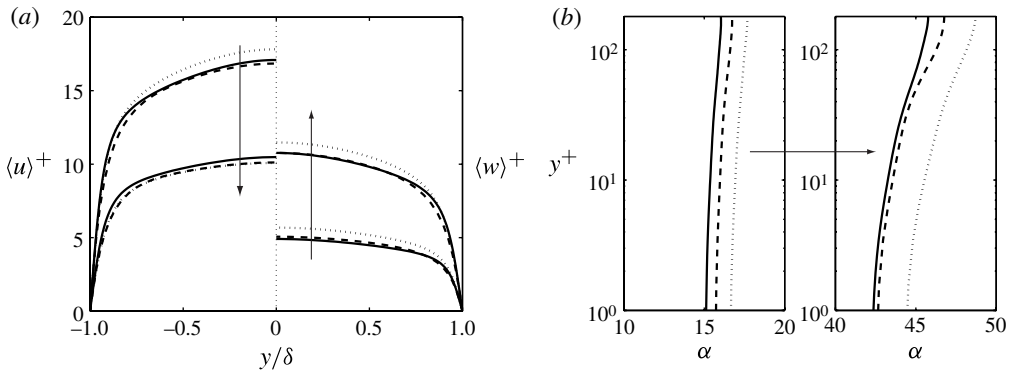


FIGURE 14. (*a*) Mean streamwise (left half) and spanwise (right half) velocity profiles normalized with the friction velocity. (*b*) Angle of the mean velocity vector relative to the streamwise direction, α, as a function of the distance from the wall for $Ro_\tau = 0.018$ (left part) and $Ro_\tau = 0.054$ (right part). Arrows point in the direction of increasing rotation rate. DNS, solid line; EASSM, dashed line; DEVM, dotted line.

rotation decreases the total heat transfer; see figure 13(*j*). The degree of the inclination of the streaky structures of the velocity and scalar fluctuations in the near-wall region depends on the magnitude of the rotation rate (Li & Liu 2006).

The third and fourth rows of figure 13 show LES predictions. The streak spacings, which can be deduced approximately from the LES predictions in these figures, are apparently larger than those from the DNS. This fact has been pointed out earlier (see e.g. Rasam *et al.* 2011*a*), which can also be statistically proven by comparing the two-point correlation data from LES and those of the DNS. The streaky structures in the spanwise velocity fluctuation are similar to those of the streamwise velocity fluctuations in both DNS and LES predictions, although, in the LES, the structures tend to be both wider and more elongated than in the DNS. The larger streak spacing in LES indicates insufficient resolution to properly represent the streaks, and the longer correlations observed from the longer structures can be attributed to the fact that the SGS contribution from the models is too statistically coherent and lacks stochastic contributions. The EASSM and the DEVM predictions are similar in that respect, although the structures predicted by the DEVM appear to be slightly shorter than those of the EASSM. The scalar fluctuations predicted by the LES are less intermittent than the DNS, which can be attributed to the same reasons as mentioned for the velocity fluctuations and both model predictions of the near-wall structures are similar.

7.2. *Mean velocity and turbulent kinetic energy profiles*

Rotational effects enter the Navier–Stokes equations through the Coriolis force; see (2.1). In the spanwise velocity equation, the force is a source term, i.e. $2\Omega\widetilde{u}_1$, and increases the spanwise velocity, while it appears as a sink term in the streamwise velocity equation, i.e. $-2\Omega\widetilde{u}_3$. Therefore, wall-normal rotation tilts the mean velocity towards the spanwise direction. Figure 14(*a*) shows the mean velocity profiles, normalized with the friction velocity, and compares the EASSM and the DEVM predictions with the DNS data. It shows that the mean streamwise velocity decreases with increasing rotation, while the spanwise velocity increases. The velocity profiles in both directions become flatter at the core of the channel as the rotation increases. The

https://doi.org/10.1017/jfm.2013.81 Published online by Cambridge University Press

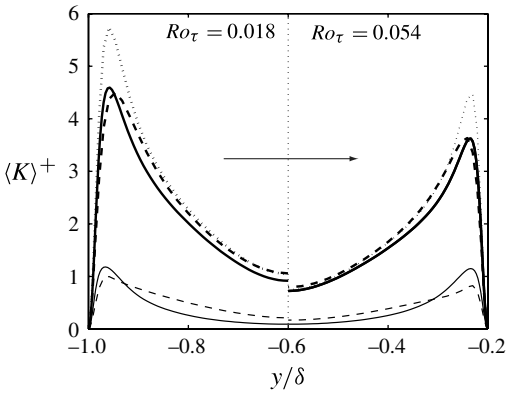


FIGURE 15. Resolved (thick lines) and SGS (thin lines) kinetic energy in wall units for $Ro_\tau = 0.018$ (left half) and $Ro_\tau = 0.054$ (right half). Filtered DNS, solid line; EASSM, dashed line; DEVM, dotted line. The arrow points in the direction of increasing rotation.

tilting angle of the mean velocity relative to the streamwise direction increases with increasing rotation rate; see figure 14(*b*).

At the higher rotation rate ($Ro_\tau = 0.054$), the bulk velocity in the streamwise direction is reduced substantially and the two SGS model predictions are similar for the streamwise velocity profile. At the lower rotation rate ($Ro_\tau = 0.018$) though, the EASSM predicts the mean streamwise velocity profile better than the DEVM; see figure 14(*a*). The spanwise velocity profiles are over-predicted by the DEVM at both rotation rates, while the EASSM predictions are in good agreement with the DNS data. The better predictions of the EASSM for the mean velocities lead to a better prediction of the mean velocity inclination, while the DEVM over-predicts it, and its prediction becomes worse with increasing rotation rate; see figure 14(*b*).

The resolved and SGS kinetic energies are shown in figure 15. The EASSM predictions of the resolved kinetic energy are in good agreement with the filtered DNS data at both rotation rates, while the DEVM over-predicts the resolved kinetic energy. The SGS kinetic energy is also satisfactorily predicted by the EASSM, while the DEVM contribution is lumped in the pressure term and is unknown. The percentages of the unresolved turbulent kinetic energy of the total kinetic energy are 18.6 and 15.0 % for the low and high rotation rates, respectively. This resolution is a moderate resolution for LES. Coarser resolutions can be used for this type of simulation with the EASSM, with satisfactory results. Rasam *et al.* (2011*a*) used coarser resolutions with the EASSM, where the SGS kinetic energy was up to 30 % of the total kinetic energy, and showed that the model performance is satisfactory, but the DEVM performance was poor at such resolutions. The reason to choose this resolution is to better resolve the velocity statistics so that model performances for the scalar predictions can be better interpreted.

7.3. *Mean and root-mean-square profiles of the scalar*

Rotational effects do not appear directly in the governing equations of the passive scalar but they affect the scalar dynamics through their influences on the velocity. Similar to the non-rotating cases, the mean scalar profile follows a logarithmic behaviour in the outer region according to (5.1) and a linear one in the diffusive sublayer; see figure 16(*a*). The slope of the logarithmic line increases with increasing

https://doi.org/10.1017/jfm.2013.81 Published online by Cambridge University Press

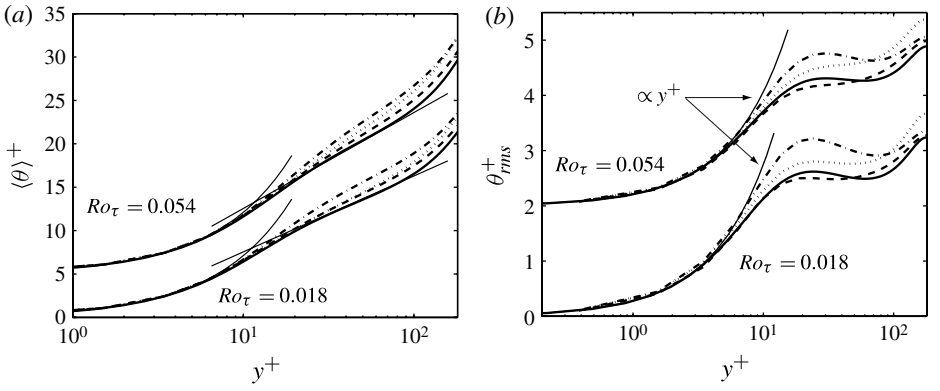


FIGURE 16. (*a*) Mean scalar and (*b*) r.m.s. of scalar in wall units for two rotation rates. DNS, solid line; EA–EA model, dashed line; ED–EA model, dash dotted line, ED–EV model, dotted line. Thin solid lines: linear profile $\langle\theta\rangle^+ = y^+Pr$ and the logarithmic law $\langle\theta\rangle^+ = (1/\kappa_T)\ln y^+ + B_T$. The mean and the r.m.s. profiles at $Ro_\tau = 0.054$ are shifted in the ordinate direction by 5 and 2 wall units, respectively, for clarity of the plots.

rotation rate (see also Li & Liu 2006). The values for the von Kármán constant and the B_T coefficient fitting the DNS data for $Ro_\tau = 0.018$ are $\kappa_T \approx 0.26$ and $B_T = -1.63$, and for $Ro_\tau = 0.054$ the corresponding values are $\kappa_T \approx 0.21$ and $B_T = -3.48$.

The EA–EA model predicts the mean scalar profile better than both the ED–EA and ED–EV models for the higher rotation rate (see figure 16*a*), while its prediction is comparable to that of the ED–EV model at the lower rotation rate.

The r.m.s. profiles of the scalar are shown in figure 16(*b*). As the rotation rate increases, the location of the near-wall peak moves away from the wall and its magnitude also increases. Li & Liu (2006) showed that the r.m.s. profile for the scalar goes linearly to zero with y^+, independent of the rotation rate, which is also shown in figure 16(*b*).

The new model predictions are in better agreement with the DNS data than the DEDM at both rotation rates. The ED–EA model largely over-predicts the near-wall peak in the r.m.s. profile. The ED–EV model gives better predictions than the ED–EA model for the latter case, but the EA–EA model predictions are closer to the DNS data.

7.4. *Mean resolved scalar fluxes and their budget*

To clarify the rotational effects on the scalar fluxes, it is useful to discuss the budget of the transport equations of the mean resolved scalar fluxes in a rotating frame of reference,

$$0 = P_{i\theta} + D_{i\theta} + \Pi_{i\theta} + \varepsilon_{i\theta} + \varepsilon^{SGS}_{i\theta} + R_{i\theta}, \tag{7.1}$$

where $P_{i\theta}$ is the production,

$$P_{i\theta} = -\langle u_i' u_j' \rangle \frac{\partial \langle\widetilde{\theta}\rangle}{\partial x_j} - \langle u_j' \theta' \rangle \frac{\partial \langle\widetilde{u}_i\rangle}{\partial x_j}. \tag{7.2}$$

$D_{i\theta}$ is the sum of the mean molecular and turbulent diffusion, $\Pi_{i\theta}$ is the mean pressure scalar-gradient correlation, $\varepsilon_{i\theta}$ is the mean molecular dissipation, $\varepsilon^{SGS}_{i\theta}$ is the SGS

https://doi.org/10.1017/jfm.2013.81 Published online by Cambridge University Press

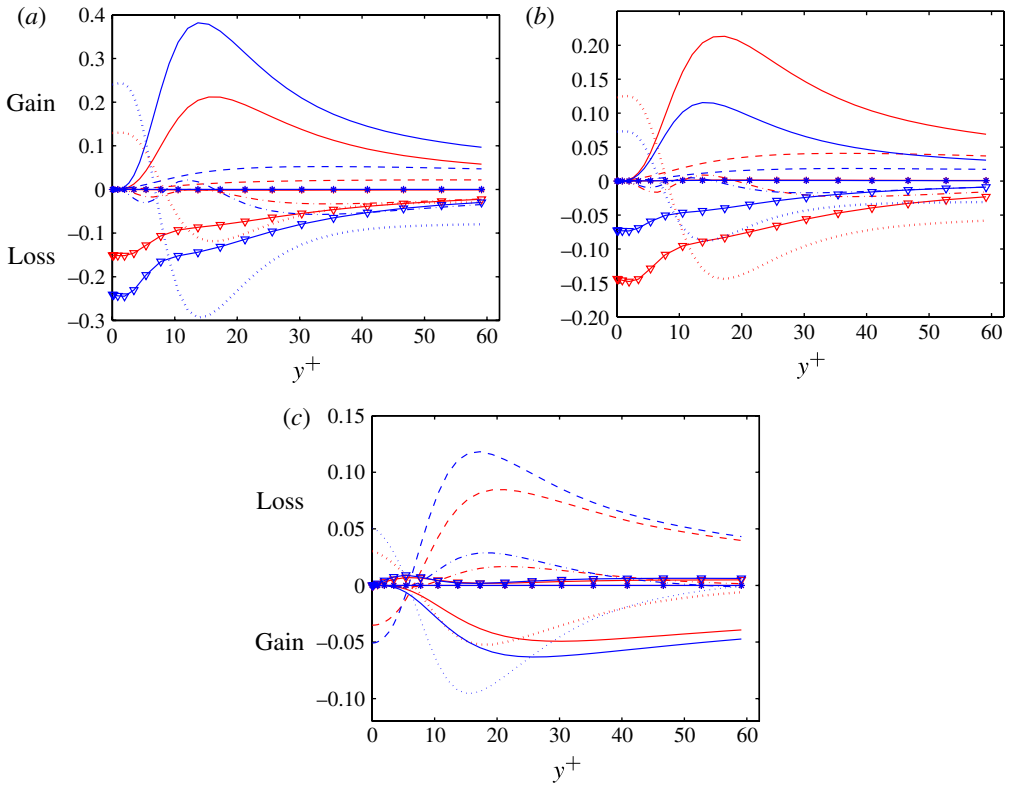


FIGURE 17. Budget terms of the mean resolved scalar fluxes, $\langle u_i'\theta'\rangle^+$, in ($a$) streamwise, ($b$) spanwise and ($c$) wall-normal directions, in wall units. Curves: ——, $P_{i\theta}$; − − −, $\Pi_{i\theta}$; − ∗ −, $R_{i\theta}$; − · −, $\varepsilon_{i\theta}^{SGS}$; − ▽ −, $\varepsilon_{i\theta}$; · · ·, $D_{i\theta}$. Blue and red lines correspond to case 5 ($Ro_\tau = 0.018$) and case 6 ($Ro_\tau = 0.054$), respectively.

dissipation and $R_{i\theta}$ is the production due to the imposed system rotation, i.e.

$$R_{i\theta} = -2\Omega_k \epsilon_{ikj} \langle u_j' \theta' \rangle, \tag{7.3}$$

$$\Pi_{i\theta} = \frac{1}{\rho} \left\langle p' \frac{\partial \theta'}{\partial x_i} \right\rangle, \tag{7.4}$$

$$\varepsilon_{i\theta} = -\left(\nu + \frac{\nu}{Pr}\right) \left\langle \frac{\partial u_i'}{\partial x_j} \frac{\partial \theta'}{\partial x_j} \right\rangle, \tag{7.5}$$

$$\varepsilon_{i\theta}^{SGS} = \left\langle q_j' \frac{\partial u_i'}{\partial x_j} \right\rangle + \left\langle \tau_{ij}' \frac{\partial \theta'}{\partial x_j} \right\rangle, \tag{7.6}$$

$$D_{i\theta} = \frac{\partial}{\partial x_j} \left(-\frac{\delta_{ij}}{\rho} \langle p'\theta' \rangle - \langle u_j' u_i' \theta' \rangle + \nu \left\langle \theta' \frac{\partial u_i'}{\partial x_j} \right\rangle + \frac{\nu}{Pr} \left\langle u_i' \frac{\partial \theta'}{\partial x_j} \right\rangle - \langle u_i' q_j' \rangle - \langle \theta' \tau_{ij}' \rangle \right), \tag{7.7}$$

where primed quantities are the resolved fluctuations.

Budgets of the resolved scalar fluxes computed from DNS data of cases 5 and 6 are shown in figure 17(a–c). The DNS data are filtered to the LES resolution of cases 1–4. The resolved plus modelled scalar fluxes for the LES and DNS predictions corresponding to cases 1–6 are shown in figure 18(a–c).

https://doi.org/10.1017/jfm.2013.81 Published online by Cambridge University Press

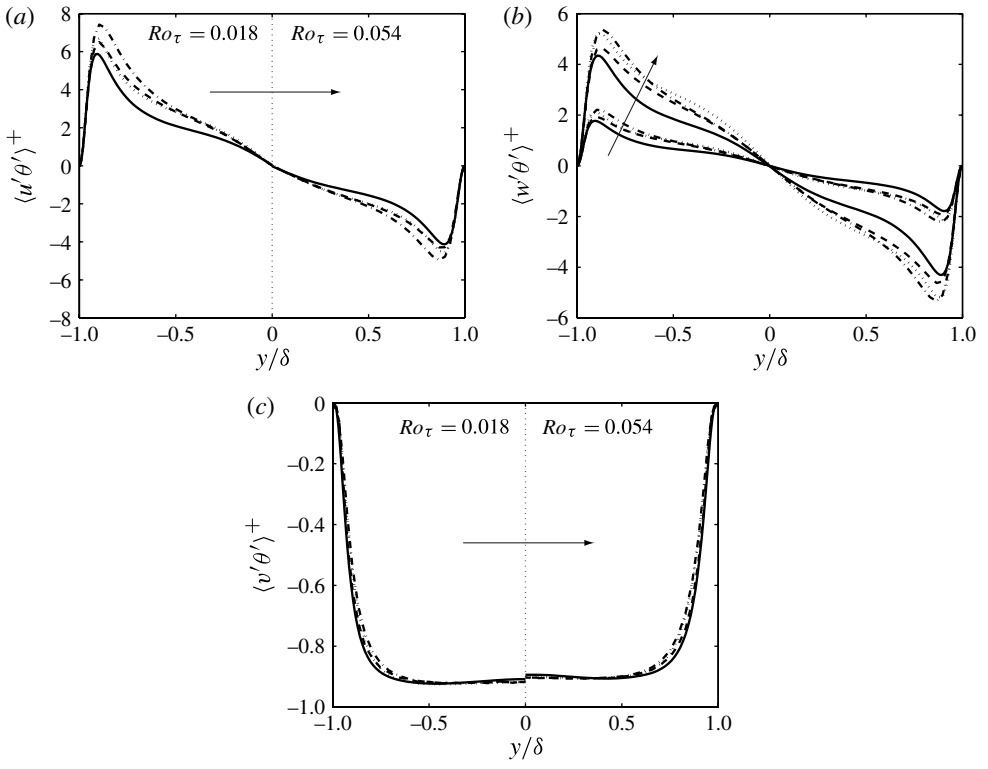


FIGURE 18. (*a*) Resolved plus modelled streamwise $\langle u'\theta'\rangle^+$ scalar flux in wall units for $Ro_\tau = 0.018$ (left half) and $Ro_\tau = 0.054$ (right half). (*b*) Resolved plus modelled spanwise $\langle w'\theta'\rangle^+$ scalar fluxes in wall units for two rotation rates. (*c*) Resolved plus modelled wall-normal scalar flux, $\langle v'\theta'\rangle^+$, in wall units for $Ro_\tau = 0.018$ (left half) and $Ro_\tau = 0.054$ (right half). DNS, solid line; EA–EA model, dashed line; ED–EA model, dash-dotted line; ED–EV model, dotted line. The arrows point in the direction of increasing rotation.

The production of the streamwise scalar flux, $\langle u'\theta'\rangle$, depends on $\langle u'v'\rangle$ and the mean streamwise velocity gradient, i.e. $P_{1\theta} = -\langle u'v'\rangle\partial\langle\widetilde{\theta}\rangle/\partial y - \langle v'\theta'\rangle\partial\langle\widetilde{u}\rangle/\partial y$; see (7.2). Rotation reduces the streamwise velocity gradient and consequently reduces $\langle u'v'\rangle$. Therefore, a reduction of the production of $\langle u'\theta'\rangle$ with increasing rotation is expected; see figure 17(*a*). The reduced production decreases $\langle u'\theta'\rangle$, which can indeed be seen in figure 18(*a*). The spanwise flux, $\langle w'\theta'\rangle$, and its budget terms are zero in a non-rotating channel flow. However, rotation induces a spanwise velocity gradient and creates $\langle v'w'\rangle$. Therefore, it produces $\langle w'\theta'\rangle$, since $P_{3\theta} = -\langle v'w'\rangle\partial\langle\widetilde{\theta}\rangle/\partial y - \langle v'\theta'\rangle\partial\langle\widetilde{w}\rangle/\partial y$; see figure 17(*b*). Rotation also affects the production of scalar fluxes through $R_{i\theta}$; see (7.3). Since the rotation numbers used here are small, the contribution of this term to the resolved scalar flux production is negligible; see figure 17(*a–c*). The correlation $\Pi_{i\theta}$ gives a positive contribution in the budgets, for both the streamwise and spanwise scalar fluxes. Rotation decreases $\Pi_{1\theta}$ but it increases $\Pi_{3\theta}$. The SGS dissipation, $\varepsilon_{i\theta}^{SGS}$, in the streamwise and spanwise directions is almost equal to the molecular dissipation, $\varepsilon_{i\theta}$, above the buffer layer, while it is negligible in comparison to $\varepsilon_{i\theta}$ in the buffer layer. The streamwise components of $\varepsilon_{i\theta}^{SGS}$ and $\varepsilon_{i\theta}$ both decrease with increasing rotation, while their spanwise component increases with increasing rotation.

https://doi.org/10.1017/jfm.2013.81 Published online by Cambridge University Press

Both $P_{2\theta}$ and $\Pi_{2\theta}$ decrease with increasing rotation rate; see figure 17(*c*). The production term, $P_{2\theta} = -\langle v'v'\rangle \partial\langle\widetilde{\theta}\rangle/\partial y$, declines with increasing rotation, due to the reduction of $\langle v'v'\rangle$. Therefore, $\langle v'\theta'\rangle$ decreases with increasing rotation rate, although its change is much less than that of the other components; see figure 18(*c*). The change of $\varepsilon_{2\theta}$ with rotation is small whereas $\varepsilon_{2\theta}^{SGS}$ decreases with increasing rotation.

The predictions of the ED–EV model for $\langle u'\theta'\rangle$ are comparable to those of the EA–EA model, while the ED–EA model gives a large over-prediction of this component. The EA–EA model predicts the $\langle v'\theta'\rangle$ flux slightly better than the other models close to the wall; see figure 18(*c*). The EA–EA model predicts $\langle w'\theta'\rangle$ better than the ED–EA and ED–EV models, especially at the higher rotation rate; see figure 18(*b*). The ED–EA and ED–EV models show a much larger over-prediction at the higher rotation rate, although the DEDM does not predict any SGS scalar flux in that direction, while the EASSFM's prediction has been added to the resolved one.

7.5. *SGS scalar fluxes*

SGS scalar fluxes are shown in figure 19(*a–c*). Similar to the resolved scalar fluxes, rotation induces an SGS scalar flux in the spanwise direction, $\langle q_3\rangle$, whereas it decreases the streamwise SGS flux, $\langle q_1\rangle$. The increase of $\langle q_3\rangle$ and the decrease of $\langle q_1\rangle$ are due to the changes in their production; see (3.2). Hence, the effect of the rotation on the SGS fluxes is similar to its effect on the resolved fluxes.

Since the DEDM assumes an alignment between the SGS flux vector and the resolved scalar-gradient vector, it predicts zero streamwise and spanwise SGS scalar fluxes. The ED–EA model fails to predict the near-wall peak of the wall-normal SGS scalar flux $\langle q_2\rangle$ at both rotation rates. The ED–EV model under-predicts the near-wall peak of $\langle q_2\rangle$ in both cases but its predictions are better than those of the ED–EA model. However, as the rotation rate increases, its prediction approaches that of the ED–EA model. The under-prediction of $\langle q_2\rangle$ by the DEDM leads to a low SGS dissipation value. The predictions by the DEDM are similar for both rotation rates.

In contrast, the new EA–EA model predicts the streamwise and spanwise SGS fluxes in good agreement with the DNS. It can predict the decrease in $\langle q_1\rangle$ and the increase in $\langle q_3\rangle$ due to rotation correctly. The new model over-predicts the wall-normal SGS flux, but it can capture the trend and the near-wall peak of this component.

8. Conclusions

A new explicit algebraic subgrid scalar flux model (EASSFM) is proposed based on a modelled transport equation for the subgrid scalar flux. The new model is based on the same kind of methodology that leads to the explicit algebraic scalar flux model (EASFM) for the Reynolds-averaged flux by Wikström *et al.* (2000). Our paper is a continuation of the work of Marstorp *et al.* (2009), who derived an explicit algebraic subgrid stress model (EASSM). The formulation of the new model is such that its prediction of the subgrid-scale (SGS) scalar flux vector is not necessarily aligned with the resolved scalar gradient vector. It uses the SGS stress tensor in its formulation, which is in agreement with the recent findings of Chumakov (2008), where it was pointed out that the direction of the SGS scalar flux vector is connected to the eigenvalues and eigenvectors of the SGS stress tensor. Since the new model includes the rotation-rate tensor in its formulation, it accounts for rotational effects at the SGS level in a natural way.

The performance of the new model was tested in non-rotating and wall-normal rotating turbulent channel flows at friction Reynolds numbers $Re_\tau = 590$ and 180,

https://doi.org/10.1017/jfm.2013.81 Published online by Cambridge University Press

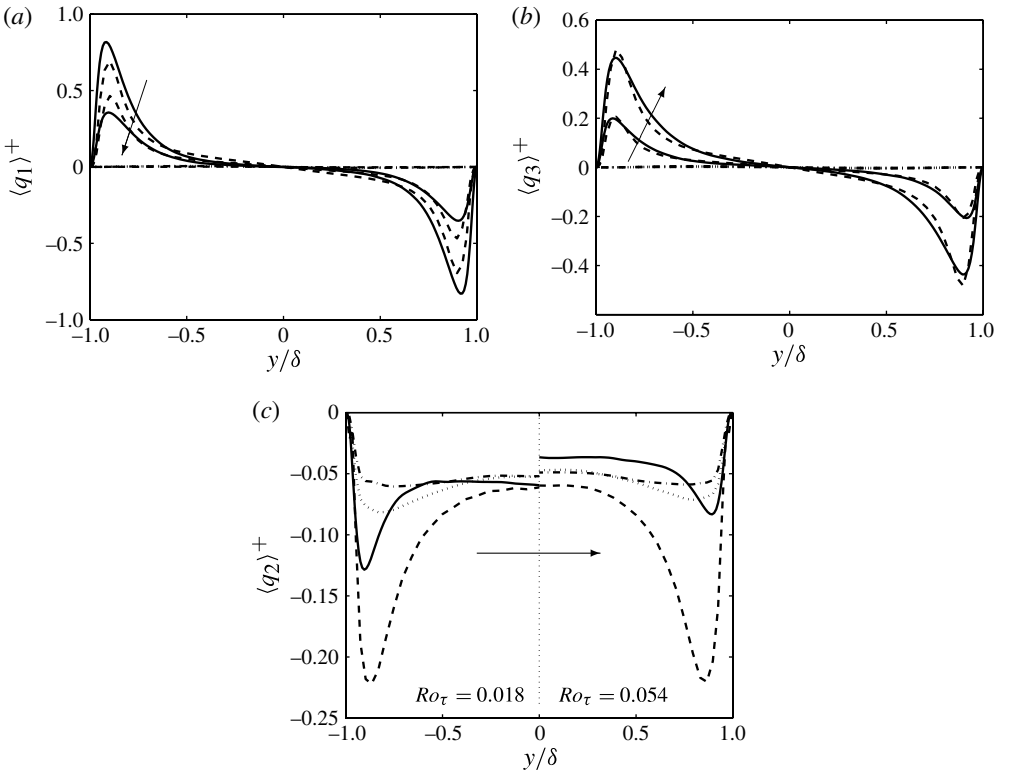


FIGURE 19. (*a*) Streamwise and (*b*) spanwise SGS scalar fluxes in wall units for two rotation rates. (*c*) Wall-normal SGS scalar flux in wall units for $Ro_\tau = 0.018$ (left half) and $Ro_\tau = 0.054$ (right half). DNS, solid line; EA–EA model, dashed line; ED–EA model, dash-dotted line; ED–EV model, dotted line. The arrows point in the direction of increasing rotation.

respectively. In both cases, the new model provided for a realistic description of the individual SGS scalar fluxes. In the case of the non-rotating channel flow, the new model was able to satisfactorily reproduce the streamwise SGS scalar flux, while the dynamic eddy diffusivity model (DEDM) failed to predict it. This advantage of the new model was more prominent in the case of the channel flow with wall-normal rotation, where it predicted both the streamwise and the spanwise SGS fluxes in good agreement with the filtered DNS data, while the DEDM predicted zero fluxes in those directions.

In the non-rotating channel flow, when the DEDM was used with the EASSM, it was found that, in comparison to this model, the new model predicted the mean scalar profiles and the resolved scalar fluxes better. When the DEDM was used with the dynamic eddy viscosity model (DEVM) for the SGS stresses, it was found that its predictions and those of the new model were comparable for the resolved quantities. However, the DEVM under-predicted the wall shear stress in comparison with the DNS and the EASSM. In the rotating flow cases, the new model improved the prediction of the mean scalar profile and the resolved scalar fluxes, especially in the spanwise direction. The improvements were more pronounced at the higher rotation rate.

https://doi.org/10.1017/jfm.2013.81 Published online by Cambridge University Press

The performance of the new model for the prediction of wall heat transfer was also tested at various resolutions. The model predictions were much closer to the DNS at various resolutions in comparison with the DEDM. Its predictions were also much less resolution-dependent, which is consistent with our previous results (Rasam *et al.* 2011*a*,*b*) for the prediction of the wall friction using the EASSM in comparison with the DEVM.

The SGS activity parameter proposed by Geurts & Fröhlich (2002) for assessment of SGS stress models was extended to the SGS scalar flux modelling. This parameter is the ratio between SGS and total dissipation of kinetic energy or scalar intensity. Therefore, it shows the relative contribution of SGS models to the total energy dissipation. Using this approach, the new model predictions were satisfactory. It provides for a smaller activity at fine resolutions, while the error in its predictions of the resolved scalar intensity becomes smaller, which is a good characteristic for an LES model.

Similar to the analysis by Kang & Meneveau (2001), we analysed the anisotropy of the SGS scalar dissipation for the non-rotating channel flow simulations. We found that the new model improves the prediction of anisotropy with respect to the DEDM, which is a consequence of the better formulation of the model in representing the SGS scalar fluxes.

A preliminary analysis of the relative computational cost of the explicit algebraic models shows that the EASSM requires around 5 % additional computational cost in comparison with the DEVM. In the LESs presented in this paper, we used the EASSFM with the EASSM, which enabled us to make use of the quantities that are already computed in the EASSM, e.g. the SGS time scale. This is another reason to use the two explicit algebraic SGS models together. The additional computational cost of the EA–EA model in comparison with the EV–ED model is around 10 %. However, the additional computational cost and complexity of the EA–EA model are balanced by the more appealing performance of the new model at coarse resolutions relative to the conventional ED–EV model. Finally, although the current study demonstrates the potentials of the explicit algebraic model for LES predictions, LESs of more complex flows have to be carried out to fully validate the new model.

Acknowledgements

The authors would like to thank Dr Linus Marstorp for his contribution to the earlier versions of the model through his PhD thesis work. We would also like to thank Dr S. Wallin for fruitful discussions on the content of the paper. Support from the Swedish Research Council through grant number 621-2010-6965 and computer time provided by the Swedish National Infrastructure for Computing (SNIC) are gratefully acknowledged.

REFERENCES

ABE, H. & ANTONIA, R. A. 2009 Near-wall similarity between velocity and scalar fluctuations in a turbulent channel flow. *Phys. Fluids* **21**, 025109.

BAGGETT, J. S., JIMÉNEZ, J. & KRAVCHENKO, A. G. 1997 Resolution requirements in large-eddy simulations of shear flows. In *Annual Research Briefs* (ed. P. Moin), pp. 51–66. Center for Turbulence Research, Stanford University.

BARDINA, J., FERZIGER, J. H. & REYNOLDS, W. C. 1989 Improved subgrid-scale models for large-eddy simulation. *AIAA Paper* 80-1357.

BATCHELOR, G. K. 1949 Diffusion in a field of homogeneous turbulence. *Austral. J. Sci. Res.* **2** (4), 437–450.

https://doi.org/10.1017/jfm.2013.81 Published online by Cambridge University Press

BRADSHAW, P. & HUANG, G. P. 1995 The law of the wall in turbulent flow. *Proc. R. Soc. Lond.* A **451**, 165–188.

CANUTO, C., HUSSAINI, M. Y., QUARTERONI, A. & ZANG, T. A. 1988 *Spectral Methods in Fluid Dynamics*. Springer.

CHEVALIER, M., SCHLATTER, P., LUNDBLADH, A. & HENNINGSON, D. S. 2007 SIMSON a pseudo-spectral solver for incompressible boundary layer flows. *Tech. Rep.* 2007:07. KTH Mechanics, Stockholm.

CHOI, H. & MOIN, P. 2012 Grid-point requirements for large eddy simulation: Chapman's estimate revisited. *Phys. Fluids* **24**, 011702.

CHUMAKOV, S. 2008 *A priori* study of subgrid-scale flux of a passive scalar in isotropic homogeneous turbulence. *Phys. Rev.* E **78**, 036313.

CLARK, R. A., FERZIGER, J. H. & REYNOLDS, W. C. 1979 Evaluation of subgrid-scale models using an accurately simulated turbulent flow (part 1). *J. Fluid Mech.* **91**, 1–16.

DAVIDSON, L. 2009 Large eddy simulations: how to evaluate resolution. *Intl J. Heat Fluid Flow* **30**, 1016–1025.

DEBUSSCHERE, B. & RUTLAND, C. J. 2004 Turbulent scalar transport mechanisms in plane channel and Couette flows. *Intl J. Heat Mass Transfer* **47**, 1771–1781.

GATSKI, T. B. & WALLIN, S. 2004 Extending the weak-equilibrium condition for algebraic Reynolds stress models to rotating and curved flows. *J. Fluid Mech.* **518**, 147–155.

GERMANO, M. 1992 Turbulence: the filtering approach. *J. Fluid Mech.* **238**, 325–336.

GERMANO, M., PIOMELLI, U., MOIN, P. & CABOT, W. H. 1991 A dynamic subgrid-scale eddy viscosity model. *Phys. Fluids* A **3** (7), 1760–1765.

GEURTS, B. J. & FRÖHLICH, J. 2002 A framework for predicting accuracy limitations in large-eddy simulation. *Phys. Fluids* **14**, L41–L44.

GHOSAL, S., LUND, T. S., MOIN, P. & AKSELVOLL, K. 1995 A dynamic localization model for large-eddy simulation of turbulent flows. *J. Fluid Mech.* **286**, 229–255.

GRUNDESTAM, O., WALLIN, S. & JOHANSSON, A. V. 2005 An explicit algebraic Reynolds stress model based on a nonlinear pressure strain rate model. *Intl J. Heat Fluid Flow* **26**, 732–745.

HIGGINS, C. W., PARLANGE, M. B. & MENEVEAU, C. 2004 The heat flux and the temperature gradient in the lower atmosphere. *Geophys. Res. Lett.* **31**, L22105.

JIMÉNEZ, C., DUCROS, F., CUENOT, B. & BÉDAT, B. 2001*a* Subgrid scale variance and dissipation of a scalar field in large eddy simulations. *Phys. Fluids* **13**, 1748–1754.

JIMÉNEZ, C., VALIÑO, L. & DOPAZO, C. 2001*b* *A priori* and *a posteriori* tests of subgrid scale models for scalar transport. *Phys. Fluids* **13**, 2433–2436.

JOHANSSON, A. V. & WIKSTRÖM, P. M. 1999 DNS and modelling of passive scalar transport in turbulent channel flow with a focus on scalar dissipation rate modelling. *Flow Turbul. Combust.* **63**, 223–245.

KADER, B. A. & YAGLOM, A. M. 1972 Heat and mass transfer laws for fully turbulent wall flows. *Intl J. Heat Mass Transfer* **15**, 2329–2351.

KANG, H. S. & MENEVEAU, C. 2001 Passive scalar anisotropy in a heated turbulent wake: new observations and implications for large-eddy simulations. *J. Fluid Mech.* **442**, 161–170.

KANG, H. S. & MENEVEAU, C. 2002 Universality of large eddy simulation model parameters across a turbulent wake behind a heated cylinder. *J. Turbul.* **3**, N32.

KAWAMURA, H., OHSAKA, K., ABE, H. & YAMAMOTO, K. 1998 DNS of turbulent heat transfer in channel flow with low to medium-high Prandtl number fluid. *Intl J. Heat Fluid Flow* **19**, 482–491.

KIM, J., MOIN, P. & MOSER, R. 1987 Turbulence statistics in fully developed channel flow at low Reynolds number. *J. Fluid Mech.* **177**, 133–166.

LESIEUR, M. & MÉTAIS, O. 1996 New trends in large-eddy simulations of turbulence. *Annu. Rev. Fluid Mech.* **28**, 45–82.

LI, B.-Y., LIU, N.-S. & LU, X.-Y. 2006 Direct numerical simulation of wall-normal rotating turbulent channel flow with heat transfer. *Intl. J. Heat Mass Transfer* **49**, 1162–1175.

LILLY, D. K. 1992 A proposed modification of the Germano subgrid-scale closure method. *Phys. Fluids* A **4** (3), 633–635.

https://doi.org/10.1017/jfm.2013.81 Published online by Cambridge University Press

LUNDBLADH, A., HENNINGSON, D. S. & JOHANSSON, A. V. 2004 An efficient spectral integration method for the solution of the Navier–Stokes equations. *Tech. Rep.* Aeronautical Research Institute of Sweden, Bromma.

MARSTORP, L., BRETHOUWER, G., GRUNDESTAM, O. & JOHANSSON, A. V. 2009 Explicit algebraic subgrid stress models with application to rotating channel flow. *J. Fluid Mech.* **639**, 403–432.

MARSTORP, L., BRETHOUWER, G. & JOHANSSON, A. V. 2007 A stochastic subgrid model with application to turbulent flow and scalar mixing. *Phys. Fluids* **19**, 035107.

MEHDIZADEH, A. & OBERLACK, M. 2010 Analytical and numerical investigations of laminar and turbulent Poiseuille–Ekman flow at different rotation rates. *Phys. Fluids* **22**, 105104.

MENEVEAU, C. 1994 Statistics of turbulence subgrid-scale stresses: necessary conditions and experimental tests. *Phys. Fluids* **6**, 815–833.

MENEVEAU, C. & KATZ, J. 2000 Scale-invariance and turbulence models for large-eddy simulation. *Annu. Rev. Fluid Mech.* **32**, 1–32.

MENEVEAU, C., LUND, T. S. & CABOT, W. H. 1996 A Lagrangian dynamic subgrid-scale model of turbulence. *J. Fluid Mech.* **319**, 353–385.

MOIN, P. & KIM, J. 1982 Numerical investigation of turbulent channel flow. *J. Fluid Mech.* **118**, 341–377.

MOIN, P., SQUIRES, K., CABOT, W. & LEE, S. 1991 A dynamic subgrid-scale model for compressible turbulence and scalar transport. *Phys. Fluids* A **3**, 2746–2757.

MONIN, P. S. 1965 On the symmetry of turbulence in the surface layer of air. *Izv. Akad. Nauk SSSR Atmos. Ocean. Phys.* **1**, 45–54.

MOSER, R. D., KIM, J. & MANSOUR, N. N. 1999 Direct numerical simulation of turbulent channel flow up to $Re_\tau = 590$. *Phys. Fluids* **11** (4), 943–945.

OBERLACK, M., CABOT, W., PETTERSON REIF, B. A. & WELLER, T. 2006 Group analysis, direct numerical simulation and modelling of a turbulent channel flow with streamwise rotation. *J. Fluid Mech.* **562**, 383–403.

PENG, S.-H. & DAVIDSON, L. 2002 On a subgrid-scale heat flux model for large eddy simulation of turbulent thermal flow. *Intl J. Heat Mass Transfer* **45**, 1393–1405.

PIOMELLI, U. & LIU, J. 1995 Large eddy simulation of rotating channel flows using a localized dynamic model. *Phys. Fluids* **7** (4), 839–848.

POPE, S. B. 2000 *Turbulent Flows*. Cambridge University Press.

PORTÉ-AGEL, F., PAHLOW, M., MENEVEAU, C. & PARLANGE, M. B. 2001*a* Atmospheric stability effect on subgrid-scale physics for large-eddy simulation. *Adv. Water Resour.* **24**, 1085–1102.

PORTÉ-AGEL, F., PARLANGE, M. B., MENEVEAU, C. & EICHINGER, W. E. 2001*b* A priori field study of the subgrid-scale heat fluxes and dissipation in the atmospheric surface layer. *J. Atmos. Sci.* **58**, 2673–2698.

RASAM, A., BRETHOUWER, G., SCHLATTER, P., LI, Q. & JOHANSSON, A. V. 2011*a* Effects of modelling, resolution and anisotropy of subgrid-scales on large eddy simulations of channel flow. *J. Turbul.* **12**, N10.

RASAM, A., BRETHOUWER, G., WALLIN, S. & JOHANSSON, A. V. 2011*b* Stochastic and non-stochastic explicit algebraic models for LES. In *Proc. 7th Intl Symp. on Turbulence and Shear Flow Phenomena, Ottawa, Canada.* http://www.tsfp7.org/papers/7A2P.pdf.

RODI, W. 1972 The prediction of free turbulent boundary layers by use of a two equation model of turbulence. PhD thesis, University of London.

RODI, W. 1976 A new algebraic relation for calculating the Reynolds stresses. *Z. Angew. Math. Mech.* **56**, T219.

SAGAUT, P. 2010 *Large Eddy Simulation for Incompressible Flows: An Introduction*, 3rd edn. Springer.

SALVETTI, M. V. & BANERJEE, S. 1995 *A priori* tests of a new dynamic subgrid-scale model for finite-difference large-eddy simulations. *Phys. Fluids* **7**, 2831–2847.

SHIH, T. H. & LUMLEY, J. L. 1986 Second-order modelling of near-wall turbulence. *Phys. Fluids* **29** (4), 971–975.

https://doi.org/10.1017/jfm.2013.81 Published online by Cambridge University Press

SJÖGREN, T. & JOHANSSON, A. V. 2000 Development and calibration of algebraic nonlinear models for terms in the Reynolds stress transport equations. *Phys. Fluids* **12**, 1554–1572.

TAFTI, D. K. & VANKA, S. P. 1991 A numerical study of the effects of spanwise rotation on turbulent channel flow. *Phys. Fluids* A **3**, 642–656.

TSUBOKURA, M., KOBAYASHI, T., TANIGUCHI, N. & KOGAKI, T. 1999 Subgrid scale modelling for turbulence in rotating reference frames. *J. Wind Engng Ind. Aerodyn.* **81**, 361–375.

VOKE, P. R. 1996 Subgrid-scale modelling at low mesh Reynolds number. *Theoret. Comput. Fluid Dyn.* **8**, 131–143.

WALLIN, S. & JOHANSSON, A. V. 2000 An explicit algebraic Reynolds stress model for incompressible and compressible turbulent flows. *J. Fluid Mech.* **403**, 89–132.

WALLIN, S. & JOHANSSON, A. V. 2002 Modelling streamline curvature effects in explicit algebraic Reynolds stress turbulence models. *Intl J. Heat Fluid Flow* **23**, 721–730.

WANG, B.-C., YEE, E., BERGSTROM, D. J. & IIDA, O. 2008 New dynamic subgrid-scale heat flux models for large-eddy simulation of thermal convection based on the general gradient diffusion hypothesis. *J. Fluid Mech.* **604**, 125–163.

WIKSTRÖM, P. M., WALLIN, S. & JOHANSSON, A. V. 2000 Derivation and investigation of a new algebraic model for the passive scalar flux. *Phys. Fluids* **12**, 688–702.

WINCKELMANS, G. S., JEANMART, H. & CARATI, D. 2002 On the comparison of turbulence intensities from large-eddy simulation with those from experiment or direct numerical simulation. *Phys. Fluids* A **14**, 1809–1811.

WU, H. & KASAGI, N. 2004 Turbulent heat transfer in a channel flow with arbitrary directional system rotation. *Intl J. Heat Mass Transfer* **47**, 4579–4591.

YOSHIZAWA, A. 1988 Statistical modelling of passive-scalar diffusion in turbulent shear flow. *J. Fluid Mech.* **195**, 541–555.

YOSHIZAWA, A., TSUBOKURA, M., KOBAYASHI, T. & TANIGUCHI, N. 1996 Modelling of the dynamic subgrid-scale viscosity in large eddy simulation. *Phys. Fluids* **8**, 2254–2256.

https://doi.org/10.1017/jfm.2013.81 Published online by Cambridge University Press